University of Alberta

A Study of "Synthetic Fence Jets" Using Image Correlation Velocimetry

by

Christopher P. Apps

©

A thesis submitted to the Faculty of Graduate Studies and Research in partial fulfillment of the requirements for the degree of Master of Science.

Department of Mechanical Engineering

Edmonton, Alberta
Fall 2001

National Library of Canada
Acquisitions and Bibliographic Services
395 Wellington Street
Ottawa ON K1A 0N4
Canada

Bibliothèque nationale du Canada
Acquisitions et services bibliographiques
395, rue Wellington
Ottawa ON K1A 0N4
Canada

Your file Votre référence

Our file Notre référence

The author has granted a non-exclusive licence allowing the National Library of Canada to reproduce, loan, distribute or sell copies of this thesis in microform, paper or electronic formats.

L'auteur a accordé une licence non exclusive permettant à la Bibliothèque nationale du Canada de reproduire, prêter, distribuer ou vendre des copies de cette thèse sous la forme de microfiche/film, de reproduction sur papier ou sur format électronique.

The author retains ownership of the copyright in this thesis. Neither the thesis nor substantial extracts from it may be printed or otherwise reproduced without the author's permission.

L'auteur conserve la propriété du droit d'auteur qui protège cette thèse. Ni la thèse ni des extraits substantiels de celle-ci ne doivent être imprimés ou autrement reproduits sans son autorisation.

0-612-69486-0

Canada

University of Alberta

Library Release Form

Name of Author: Christopher P. Apps

Title of Thesis: A Study of "Synthetic Fence Jets" Using Image Correlation Velocimetry

Degree: Master of Science

Year this Degree Granted: 2001

Permission is hereby granted to the University of Alberta to reproduce single copies of this thesis and to lend or sell such copies for private, scholarly, or scientific research purposes only.

The author reserves all other publication and other rights in association with the copyright in the thesis, and except as hereinbefore provided, neither the thesis nor any substantial portion thereof may be printed or otherwise reproduced in any material form whatever without the author's prior written permission.

Chris Apps

Christopher P. Apps
11455 43 ave.
Edmonton, Alberta,
Canada. T6J 0Y2

September 28, 2001

University of Alberta

Faculty of Graduate Studies and Research

The undersigned certify that they have read, and recommend to the Faculty of Graduate Studies and Research for acceptance, a thesis entitled A Study of "Synthetic Fence Jets" Using Image Correlation Velocimetry submitted by Christopher P. Apps in partial fulfillment of the requirements for the degree of Master of Science .

Dr. L.W. Sigurdson (Supervisor)

Dr. M. Loewen

Dr. B.A. Fleck

September 28, 2001

"Is it all just smoke and mirrors?"

–unknown

Abstract

As opposed to a normal jet through an orifice, we have proposed and verified that another type of jet called a "Synthetic Fence Jet" (SFJ) can also be created. We introduced a fence perpendicular to the wall of a pipe with a standing acoustic wave in it. This phenomenon could be used as an actuator for flow control or as a mixer. The objective of this project was to use flow visualization to prove the existence of, and characterize, this jet. It has been discovered that the jet direction can be vectored along the pipe axis by altering the forcing waveform. To explain this a theory was developed that is based on the Biot-Savart law of vortex dynamics. A digital image correlation velocimetry system has been developed. It compares two images exposed at two different times by using two colours of light.

ACKNOWLEDGEMENTS

I would like to thank everybody involved in this project. To begin with I would like to thank my fellow VFD Students: Andrew Coward whose ability to get the job done has never ceased to amaze me, John Diep for his brainstorming and assistance with ideas, and Dave deJong for setting up the LaTeX code and making it more user friendly for me. I would also like to thank the summer students as well as the post-doctoral student that were involved in the project: Katherine Leicht and Michelle Vigeant, for their tireless jet searching efforts and Dr. Tony Chen for writing the ICV Code and helping me to understand it. Thanks also to my good friend Stephen Kieser who helped with many late night experiments. Special thanks to Ian Buttar and Bernie Faulkner whose knowledge and abilities are far to extensive for mere mortals. I would also like to thank machinists Dave Pape, Don Fuhr and Albert Yuen for producing the works of art that were used in the experiments.

Finally, I would like to express my gratitude to Dr. Lorenz Sigurdson who has been many things to me: supervisor, grad coordinator, course instructor, mentor and friend. I am greatly appreciative of the guidance that you have given me.

Thanks to the National Sciences and Engineering Research Council who provided the funding for this work. I would also like to thank the department of Mechanical Engineering for providing a research assistantship and the Faculty of Graduate Studies and Research for the J. Gordin Kaplin graduate student travel award as well as the tuition award.

CONTENTS

1 Introduction **1**

1.1 Introduction 1

1.1.1 Motivation 2

1.2 Theoretical Considerations 6

1.2.1 Velocity Field Decomposition 6

1.2.2 Biot-Savart Law 7

1.2.3 Vortex Roll-up 8

1.2.4 Start-up of Synthetic Fence Jet 9

1.2.5 Dimensional Analysis 10

1.3 Related Phenomena 13

1.3.1 Related Jets 13

1.3.2 Similar Phenomena 15

1.3.3 Conclusions From Review 25

1.4 Specific Objectives 25

1.5 Thesis Outline 26

Bibliography **27**

2 Synthetic Fence Jets **31**

2.1 Introduction 31

2.2 Experimental Setup and Apparatus 32

2.2.1 Pulsating Pipe Facility 32

2.2.2 Smoke Wire Flow Visualization 35

2.2.3 Timing Box and Photography 36

2.2.4 Fence Insert 37

2.2.5 Resonance Map of Pipe 41

2.3 Results and Discussion 45

2.3.1 Synthetic Fence Jet 45

2.3.2 Vectored Synthetic Fence Jet 64
2.4 Conclusions 78

Bibliography **82**

3 Image Correlation Velocimetry **83**
3.1 Introduction 83
3.2 Theory 83
3.2.1 Background and Literature Review 84
3.3 Preliminary Experiments 88
3.3.1 Double Exposure 88
3.3.2 Time Series - 'Burst Mode' on Camera 88
3.3.3 One Flash, Two Flash, Red Flash, Blue Flash 90
3.4 Dr. Tony Chen's ICV Code 100
3.4.1 Introduction 100
3.4.2 How the Code Works 100
3.5 Validation 105
3.5.1 Digitally Simulated Velocity 105
3.5.2 Rotating Disc 111
3.5.3 Normal Jet Image Correlation Velocimetry Validation . 113
3.5.4 Turbulent Pipe Flow 118
3.5.5 Validation Summary 125
3.6 Conclusions 127

Bibliography **131**

4 Conclusions and Further Research **132**
4.1 Conclusions 132
4.2 Further Research 133

Bibliography **136**

A ICV Initialization File **137**

List of Tables

2.1 Sequence Of Events Controlled By The Electronic Timing Box 37
2.2 Maxima And Minima Of Resonance Map For U'_{max} 43
2.3 Maxima And Minima Of Resonance Map For U'_{fence} 43
2.4 Map Of Parameters For Which Jetting Occurs For 25.4 mm (1") Fence 47
2.5 Map Of Parameters For Which Jetting Occurs For 12.7 mm (1/2") Fence 48

3.1 Turbulent Pipe Flow: Comparison Of Percent Error And Pixel Error 125

A.1 Sample Initialization File 138

List of Figures

1.1 2D Fence In An Oscillating Flow Field 7
1.2 Biot-Savart Law Applied To A Two Dimensional Point Vortex 8
1.3 Biot-Savart Law Applied To A Pair Of Two Dimensional Point Vortices 9
1.4 Hypothetical Startup Of Synthetic Fence Jet 11
1.5 Parameters For Dimensional Analysis 12
1.6 Acoustic Streaming In A Pipe 17
1.7 Acoustic Streaming Around A Cylinder 17
1.8 Comparison Between Oscillating Flow Past A Fence And Oscillating Flow Past A Cylinder 23

2.1 Schematic Of Pulsating Pipe Facility 33
2.2 Rendering Of Preliminary Fence Insert Assembly: Unassembled 39
2.3 Rendering Of Preliminary Fence Insert Assembly: Assembled . 39
2.4 Intermediate And Final Fence Edge Design 40
2.5 Rendering Of Final Fence Insert Assembly: Unassembled . . . 42
2.6 Rendering Of Final Fence Insert Assembly: Assembled 42
2.7 Resonance Map Of Pulsating Pipe Facility 44
2.8 ICV Photograph Of SFJ 52
2.9 ICV Result From Photograph Shown In Figure 2.8 53
2.10 Set Of ICV Results With Averaged ICV Result 54
2.11 Plot Of Velocity Ratio Against Strouhal Number For Re=620 56
2.12 Plot Of Velocity Ratio Against Strouhal Number For Re=410 57
2.13 Plot Of Velocity Ratio Against Reynolds Number For Constant Frequency Of 40 Hz 58
2.14 Chain Of Vortex Rings 60
2.15 Photograph Of SFJ Suggesting Chain Of Vortex Rings 61
2.16 Photograph Of SFJ Suggesting Chain Of Vortex Rings 62
2.17 Schematic Of Frequency Calculation 63

2.18 Bottom View Of Vectored Synthetic Fence Jet 65
2.19 Voltage Signal Produced By The Damaged Power Oscillator . 67
2.20 Pressure At Transducer P2 In The Pipe 67
2.21 Hot-Wire Voltage Trace At Fence Location With Fence Removed 68
2.22 Basic Mechanism For Synthetic Fence Jet Vectoring. 69
2.23 Generation Of Vorticity At The Fence's Edge 72
2.24 Proposed Simplified Waveform To Produce Vectored Jetting . 75
2.25 Synthesized Waveforms To Produce Vectored Jetting 78

3.1 'Burst' Photograph: First In Series 91
3.2 'Burst' Photograph: Second In Series 91
3.3 'Burst' Photograph: First In Series 92
3.4 'Burst' Photograph: Second In Series 92
3.5 Initial Stroboscope Mounting Schematic. Strobes Mounted At Approximately 75° Apart. 94
3.6 Beam Splitter Apparatus Light Schematic 97
3.7 Difference Between Red And Blue Components For Simultaneous Strobe Photograph Of The SFJ With Strobes Mounted 20° Apart 98
3.8 Difference Between Red And Blue Components For Simultaneous Strobe Photograph Of The SFJ With Beam Splitter Apparatus 98
3.9 Grid Photograph For SFJ Experiments 106
3.10 Grid Photograph For Turbulent Pipe Flow Experiments 106
3.11 Digitally Simulated Velocity: Cropping For Translation 107
3.12 Digitally Simulated Velocity: Translation ICV Result 109
3.13 Digitally Simulated Velocity: Cropping For Rotation 110
3.14 Digitally Simulated Velocity: Rotation ICV Result 112
3.15 Photograph From Spinning Disc Experiment 114
3.16 ICV Result From Spinning Disc Experiment 115
3.17 Velocity Extracted Along A Line From Spinning Disc Experiment 116
3.18 Photograph From Normal Jet Image Correlation Velocimetry Validation Experiment 117
3.19 Image Correlation Velocimetry Result From Normal Jet Image Correlation Velocimetry Validation Experiment 119
3.20 Averaged Image Correlation Velocimetry Result From Normal Jet Image Correlation Velocimetry Validation Experiment . . 120

3.21 Averaged ICV Velocity Along Centerline From Normal Jet ICV Validation Experiment. 121
3.22 Photograph From Turbulent Pipe Flow Experiment 122
3.23 Image Correlation Velocimetry Results From Turbulent Pipe Flow Experiment 123
3.24 Image Correlation Velocimetry And Hot-Wire Centerline Velocity From Turbulent Pipe Flow Experiment. 124

NOMENCLATURE

LATIN SYMBOLS

A	Area
b	distance
C	correlation
D	distance to center of vorticity
f_{ex}	frequency of velocity fluctuation
h	fence height
i	horizontal pixel location
j	vertical pixel location
k	constant
KC	Keulegan-Carpenter number $= \frac{U'_{fence}}{fh}$
R	correlation coefficient
Re	Reynolds number $= \frac{U'_{fence}D}{\nu}$
St	Strouhal number $= \frac{fh}{U'_{fence}}$
u	velocity
U'	magnitude of velocity fluctuation

$\vec{u}$ ..... velocity

$\vec{u}_d$ ..... deformation component of velocity

$\vec{u}_r$ ..... rotation component of velocity

$\vec{u}_t$ ..... translation component of velocity

v_j ..... jet velocity

v_s ..... velocity at edge of the boundary layer at separation

V ..... volume

v ..... velocity

$\bar{X}$ ..... position vector of center of vorticity

X, Y ..... coordinates of center of vorticity

$\bar{x}$ ..... position vector

$\bar{x}'$ ..... integration parameter

GREEK SYMBOLS

Γ ..... circulation

η ..... tunable parameter; distance from top of image

ν ..... kinematic viscosity

τ ..... period

ξ ..... distance from left side of image

ω ..... vorticity

subscripts:

F ..... portion of original image

$fence$ ..... at the fence location

j, jet ..... jet

L ..... left

max ..... maximum

R ..... right

T ..... template or correlation window

CHAPTER 1

INTRODUCTION

1.1 Introduction

Flow control is an increasingly important area in fluid dynamics research. Gad-el-Hak (2000) emphasizes the importance of flow control research:

> The ability to manipulate a flowfield actively or passively to effect a desired change is of immense technological importance, and this undoubtedly accounts for the subject's being more hotly pursued by scientists and engineers than any other topic in fluid mechanics.

The purpose of the research presented here was to develop a new jet actuator that might be useful for flow control. Dr. Sigurdson suggested the possibility that a jet could be created from the edge of a plate in an oscillating cross flow. This is similar to the jet resulting from a dolphin flapping its tail except that the plate would be stationary while the flow is 'flapping'. This type of

mechanism would be particularly useful in a pipe because the pipe could be used as an acoustic wave-guide. The energy of the acoustic wave could be extracted in the form of a jet by placing a plate or 'fence' at whatever locations in the pipe are desired. We have proven that this jet does in fact occur, and we will refer to it as a 'synthetic fence jet' (SFJ).

This section will begin by explaining the motivation for this research. It will then discuss in detail the theoretical considerations for the hypothesis. A literature review will be presented of phenomena that are similar to the synthetic fence jet. Finally, a set of specific objectives of the research and an outline of the thesis will be presented.

1.1.1 Motivation

1.1.1.1 Pipe Flow

In Canada approximately two thirds of our nation's energy supply is transported through pipelines. This energy consists primarily of natural gas and crude oil. Pipelines are also used for the hydrotransport of oil sands. There are two main problems associated with pumping fluids through pipelines. First there is the pressure head loss caused by friction at the pipe walls. This problem exists for all pipelines. The second problem is maintaining suspension of the solids in solid-fluid mixtures. This problem is specific to only some pipes, for example those used for the hydrotransport of oil sands.

1.1.1.2 Head Loss

There is a tremendous amount of research currently being done to try to reduce frictional losses in boundary layers. More so in the past, there has also been work on reducing pressure head loss through pipes. Some of these methods involve adding "... long-chain molecules, surface-active agents and microbubbles in liquid flows, and small solid particles and fibers in either gases or liquids." (Gad-el-Hak, 2000). Other methods involve either passively or actively interacting with the large scale structures in the turbulence.

One of the passive methods to reduce frictional losses in boundary layers is the introduction of grooves or riblets on the surface. These grooves are expected to interact with the large scale vortex structures in the boundary layer and thereby reduce the drag. Bechert and Bartenwerfer (1989) recognize that "the skin of fast sharks is covered with tiny scales which have little longitudinal ribs on their surface." They study the effects of a number of different rib geometries on boundary layer flow using conformal mapping to determine the velocity distributions. Bruse et al. (1993) performed experiments using various riblet geometries on flat plates and found drag reductions as high as 10%. It is expected that the same mechanism should also work in pipe flows. Choi et al. (1994) has used more active methods to reduce skin friction drag in turbulent boundary layers. These methods include control of the normal, spanwise and streamwise velocities at the wall. Nieuwstadt (1998) has used a similar method in pipes which involves periodic radial suction and blowing at intervals along a pipe to reduce the pressure head

loss. Some researchers have started using feedback control strategies in their attempts to reduce drag in boundary layers. In numerical simulations of turbulent boundary layers, Choi et al. (1994) apply blowing and suction at the wall that is equal and opposite to the wall-normal velocity at some distance away from the wall. More recently, Choi et al. (1998) have used suboptimal control strategies that involve using pressure or shear stress at the wall in turbulent boundary layers. This flow information is more easily obtained in real world applications. They report drag reductions of $16 - 22\%$ in their simulations. We want to try to transfer some knowledge about boundary layer control to pipes.

1.1.1.3 Solid Suspension

In oil sands hydrotransport water is mixed with the oil sands to form a slurry. This slurry is then pumped through the pipelines to transport it to a processing facility. One of the problems that occurs with this method is that the solids tend to settle out of the liquid causing restrictions in the pipelines. In order to avoid this problem the mixture is pumped at higher flow rates resulting in rapid erosion of the pipelines. Some sort of mechanism for improving the suspension of these solids in these pipelines would allow them to be pumped at lower flow rates and reduce the erosion on the pipelines. It would also be beneficial to have mixing, and therefore processing, as it is pumped down the pipeline. One idea is to use some sort of flow control mechanism to enhance the suspension of solids in these fluid solid mixtures.

A series of vertically oriented jets could be produced at regular intervals along a pipeline to potentially maintain the suspension of solids. This might allow lower flow rates through the pipelines and reduce the premature erosion. Some variation of this effect may be possible with the mechanism discussed in this thesis.

1.1.1.4 Mixing in Pipes and Chemical Reactors

Chemical reactors are used to mix chemicals and force a chemical reaction between them. It is very important that the chemicals are thoroughly mixed in order for the chemical reaction to occur completely. A new flow control mechanism to enhance mixing in chemical reactors leading to improved performance would be desirable.

1.1.1.5 Other Methods of Flow Control

The motivation for this research is to develop a new method of flow control that might be useful for the problems mentioned in Sections 1.1.1.1 through 1.1.1.4. Flow control through the use of acoustic excitation is not a new idea. Sigurdson and Roshko (1988) examined the effect of acoustic excitation on the separation bubble downstream of a "sharp-edged blunt face of a circular cylinder aligned coaxially with the free stream" and found that the reattachment length could be modified. Similar results for backward facing steps have been reported by Chun and Sung (1996), Chun and Sung (1998) and Chun et al. (1999). Choi et al. (1999) numerically investigated control

strategies for minimizing the reattachment length for a backward facing step. They used blowing and suction through the face of the step as the control mechanism. In recent years synthetic jets have been used as a flow control mechanism. Smith and Glezer (1998) have studied the use of synthetic jets to affect normal jets. More recently Diep (2001) has examined the use of synthetic jets to reduce smokestack downwash (see Section 1.3.1). We will discuss synthetic jets in more detail in Section 1.3.1.2. There are a wide variety of applications where the use of acoustic excitation as a method of flow control is being researched.

1.2 Theoretical Considerations

In this section we will explain the hypothesis and show the theory that supports it. We hypothesized that a jet could be created by placing a "fence" perpendicular to an oscillating flow field as seen in Figure 1.1. The vortices that are shed from the edges of the fence could interact with each other to form a jet of fluid moving away from the fence. In the next few sections we will show why this is expected.

1.2.1 Velocity Field Decomposition

Panton (1996) shows that a velocity field can be "...decomposed into three distinct components: a translation, a solid-bodylike rotation, and a deformation."

Figure 1.1: 2D fence in an oscillating flow field. U' and f are the amplitude and frequency of the velocity oscillation.

$$\vec{u} = \underbrace{\vec{u_t}}_{translation} + \underbrace{\vec{u_r}}_{rotation} + \underbrace{\vec{u_d}}_{deformation} \tag{1.1}$$

By decomposing the flow in this way, we can more easily look at the way in which simple flows will behave. In the next section we will examine the rotational component.

1.2.2 Biot-Savart Law

The rotational components of the flow are governed by the Biot-Savart Law of fluid dynamics. This law is related to the law of the same name in electromagnetic theory. The full equation for the Biot-Savart law is given in Equation 1.2. In this equation, $\vec{u_r}$ is the induced velocity at an arbitrary point, $\overline{x}$ is the position vector of that point, $\overline{x}'$ is the variable of integration, and ω is the vorticity. For a two dimensional point vortex as seen in Figure 1.2, this equation can be simplified and the velocity at any point A can

be found by Equation 1.3.

$$\vec{u_r} = \frac{-1}{4\pi} \int_{entirevolume} \frac{(\bar{x} - \bar{x}') \times \omega(\bar{x}')}{|\bar{x} - \bar{x}'|^3} dV(\bar{x}') \tag{1.2}$$

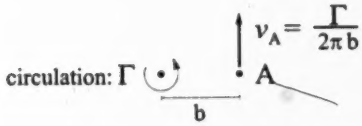

Figure 1.2: Biot-Savart law applied to a two dimensional point vortex. Γ is the circulation of the vortex. b is the distance point A is away from the vortex. v_A is the velocity at point A induced by the vortex.

$$v_A = \frac{\Gamma}{2\pi b} \tag{1.3}$$

For a pair of two-dimensional counter rotating point vortices of equal circulation as seen in Figure 1.3 the vortices propagate in a direction perpendicular to the line joining the two vortices.

1.2.3 Vortex Roll-up

Now that we understand how the vortices will behave once they exist, we must now address how they are formed. As a flow passes a sharp edge, a vortex is formed on the downstream side. This is sometimes referred to as a starting vortex or a vortex rollup. A very good example of this phenomenon can be found in Pullin and Perry (1980) who studied "...the growth of a

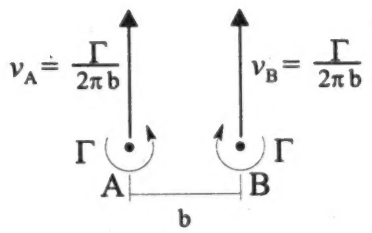

Figure 1.3: Biot-Savart law applied to a pair of two dimensional point vortices. Γ is the circulation of the vortices. b is the distance between the point vortices. v_A and v_B are the induced velocities of the vortices.

two-dimensional starting flow vortex formed at a wedge-like sharp edge." This same phenomenon would occur in the case of a sharp edged fence in an oscillating flow as seen in Figure 1.1 on Page 7.

1.2.4 Start-up of Synthetic Fence Jet

Here we will consider the initial startup of an oscillating flow past a fence on an infinite flat plate as seen in Figure 1.4(a). Initially, the velocity field is zero everywhere. As the flow begins to move to the right, a starting vortex is formed on the downwind (right) side of the fence. This is depicted in Figure 1.4(b). When the flow reverses, a vortex of opposite sign vorticity is formed also on the downwind side except that the downwind side is now the left side of the fence as shown in Figure 1.4(c). Also, the first vortex is convected with the flow. Now that there are two vortices, we must consider

the effect of the vortices on each other[1]. We apply the Biot-Savart law (see Section 1.2.2) and find that the vortices will tend to move in a vertical direction away from the fence (see Figure 1.4(d)). This direction depends on the relative position of the vortices with respect to each other so this initial pair of vortices might go off in any direction. For the sake of simplicity, we will assume that they are positioned approximately as shown in Figure 1.4(c) and (d). By applying this logic through a number of cycles we end up with a staggered arrangement of vortices as seen in Figure 1.4(h). The velocity field for this arrangement of vortices is a jet moving vertically away from the fence. Sigurdson (1986) suggested that the vortex structure of a circular jet was a chain of vortex rings. A two dimensional slice, in the correct plane, of a chain of vortex rings shows a staggered arrangement of vortices like what is shown in Figure 1.4(h).

1.2.5 Dimensional Analysis

Now that we have shown why the synthetic fence jet is expected to exist we will now examine what parameters may be important in producing this phenomenon. In order to get some sense of the relevant non-dimensional groups a dimensional analysis was performed. There are 5 parameters in the problem as seen in Figure 1.5. U' and f_{ex} are the amplitude and frequency of the oscillating velocity field. h is the height of the fence, v is the jet velocity

[1]To be completely accurate we would also have to consider the effects of the boundaries in the problem. There would be a series of image vortices that would also affect the motion of the vortices. We have chosen to neglect these effects in order to simplify the problem. Due to the distance from the boundaries, the effects would be relatively small.

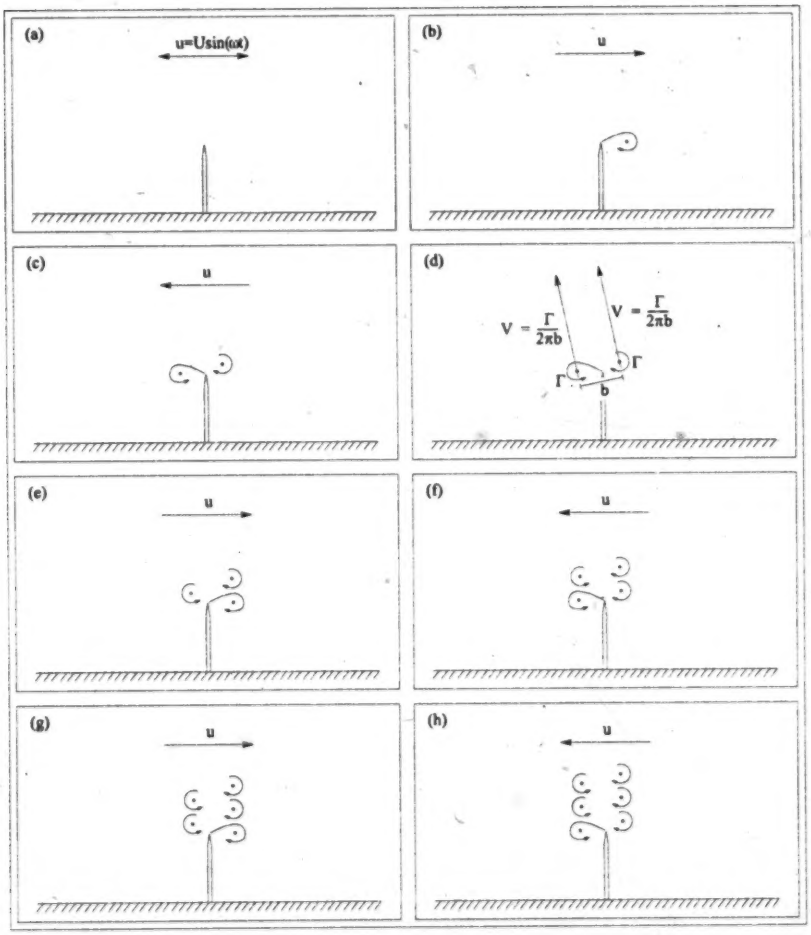

Figure 1.4: Hypothetical startup of synthetic fence jet. (a) Shows the general flow condition. (b) Starting from rest the flow begins to move to the right and a starting vortex is created to the right of the fence. (c) The flow moves to the left and a vortex of opposite sign circulation is created to the left of the fence. (d) The vortices will propagate away from the fence according to the Biot-Savart law. (e), (f) and (g) As the flow continues to oscillate, more vortices are created. (h) The result is a staggered arrangement of vortices.

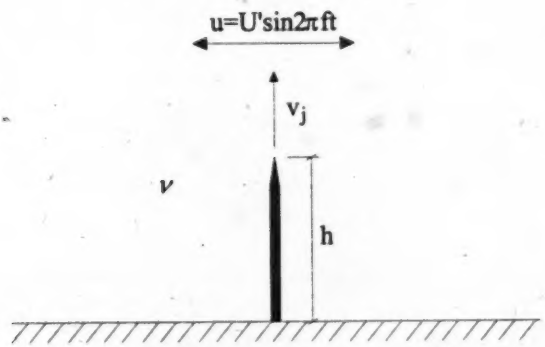

Figure 1.5: Parameters for dimensional analysis. A 2D fence on an infinite flat plate in an oscillating flow field. u is the velocity of the flow. U' and f are the amplitude and frequency of the velocity oscillation. v_j is the synthetic fence jet velocity and h is the height of the fence. ν is the kinematic viscosity of the fluid and t is time.

and ν is the kinematic viscosity of the fluid. There are only 2 dimensions in these parameters, length and time. Buckingham Pi Theorem suggests that there should be $\geq 5 - 2 = 3$ non-dimensional parameters. One possible set of non-dimensional parameters are shown in Equations 1.4 to 1.6. The most important non-dimensional parameter is expected to be the Strouhal number because it often is for oscillating flows above a critical Reynolds number. The inverse of the Strouhal number is known as the Keulegan-Carpenter number and is also often used for flows where there is an oscillation. For the purposes of this thesis we will use the Strouhal number. Only experiments can determine what the appropriate non-dimensional groups are.

$$\text{Velocity Ratio} \ldots \quad \frac{v_j}{U'} \tag{1.4}$$

$$\text{Strouhal Number} \ldots \quad St = \frac{fh}{U'} \tag{1.5}$$

$$\text{Reynolds Number} \ldots \quad Re = \frac{U'h}{\nu} \tag{1.6}$$

1.3 Related Phenomena

In this section we will present a review of phenomena that are similar to the synthetic fence jet. To begin with we will discuss other types of fluid jets that exist, followed by other types of phenomena that are related to the synthetic fence jet.

1.3.1 Related Jets

Here we present some information about types of fluid jets. The two types of jets that we will discuss are; normal fluid jets and synthetic jets.

1.3.1.1 Normal Fluid Jets

The simplest form of jet is the momentum jet. This type of jet is the most well understood and has been studied extensively. It consists of fluid passed through an orifice. Sigurdson (1986) suggests that the vortex structure of a circular jet is a chain of vortex rings. Jets with various forms of perturbations have been studied. Panton (1996) discusses how "... even acoustic perturba-

tions, at the edge, where the jet or layer is formed, can have large effects [on the jet]". Panton (1996) references Zaman and Hussain (1980) who studied the effects of plane axial acoustic perturbations on jets and found that the structure and the growth of the shear layer in the jet could be altered. Panton (1996) also references Juvet and Reynolds (1989) who found that the jet could be made to "bloom". Blooming is when the vortex rings that make up the jet leave the exit of the jet in many directions resulting in a very broad velocity profile.

1.3.1.2 Synthetic Jets

Smith and Glezer (1998) describe a synthetic jet as being "...engendered by the interaction of discrete vortical structures which are formed by time-periodic ejection of fluid out of an orifice at the flow boundary." They produce a synthetic jet by vibrating a diaphragm in a sealed cavity that has an orifice. The vortices that are shed at the edges of the orifice produce a jet of fluid outside the cavity. The orifice used was rectangular in this case but others have used circular orifices to produce the same type of phenomenon. Mallinson et al. (1999) studied a synthetic jet formed using a circular orifice. The structure of the jet produced has been noted to be very similar to that of a normal fluid jet. This type of jet has also been referred to as a form of acoustic streaming (see Section 1.3.2.1). The most important feature of a synthetic jet is that it produces a jet flow without net mass addition.

The use of synthetic jets in a variety of applications has been researched.

Smith and Glezer (1998) have found that a synthetic jet could alter the direction of normal fluid jets. Mallinson et al. (1999) studied the effect of a synthetic jet on the mixing in a flame. Diep (2001) examined the use of synthetic jets to reduce smokestack downwash. By placing an annular synthetic jet around a stack, the downwash effects could be reduced. There are a number of possible uses for synthetic jets.

1.3.2 Similar Phenomena

Here we will present a review of phenomena that are not 'jets' in the usual sense but are related to the synthetic fence jet. These phenomena include acoustic streaming, fish tail vortices and boat bilge keels. Acoustic streaming encompasses all types of flows that are caused by an acoustic wave. Fish tail vortices are created by the motion of fish tails as they swim. Boat bilge keels are used to damp the oscillations of boats. There has been research done on all of these topics and they all bear some resemblance to the synthetic fence jet.

1.3.2.1 Acoustic Streaming

"The phrase 'acoustic streaming' implies a mean motion generated by sound" (Lighthill, 1978). The synthetic fence jet would fall into this category provided that it is produced by an acoustic source. Lighthill (1978) presents an excellent review of acoustic streaming phenomena. He discusses a variety of types of acoustic streaming phenomena including the McIntyre sink, RNW

streaming and Stuart streaming.

The McIntyre sink appears to be a similar phenomenon to the synthetic jet. "An acoustic source ... generates an unattenuated narrow beam." Also, "... the balancing Eulerian mean motion outside the beam, carrying a [net] mass flow ... symmetrically inwards to the source." Lighthill (1978) states that "the velocities involved in this motion are typically very small."

According to Lighthill (1978), RNW streaming is "streaming as calculated by the method of [Rayleigh, Nyborg and Westervelt]." These forms of acoustic streaming are typically creeping motions. This is partly because one of the approximations in the analysis requires that the flow be very slow. Lighthill (1978) examines the influence of boundaries on RNW streaming and discusses Rayleigh's calculations of RNW streaming for a standing wave in a pipe. This acoustic streaming in a pipe is described as a creeping motion. The flow that is created in a pipe by an acoustic standing wave is shown in Figure 1.6. There is flow away from the velocity nodes in the center of the pipe and towards the velocity nodes near the walls of the pipe.

Lighthill (1978) also describes Rayleigh's work on the acoustic streaming around a cylinder. The flow around a circular cylinder perpendicular to an acoustic wave, of wave length much greater than the diameter of the cylinder, is a mean flow away from the cylinder parallel to the acoustic wave and a mean flow towards the cylinder perpendicular to the acoustic wave as seen in Figure 1.7.

The topic of vortical fluid motion created by oscillating flows has also

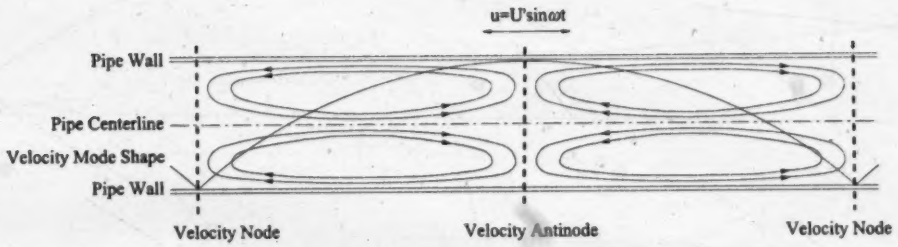

Figure 1.6: Acoustic streaming in a pipe, as discussed by Lighthill (1978). The streamlines shown are the creeping flow caused by the acoustic wave in the pipe. The nodes and antinodes refer to the acoustic velocity fluctuations.

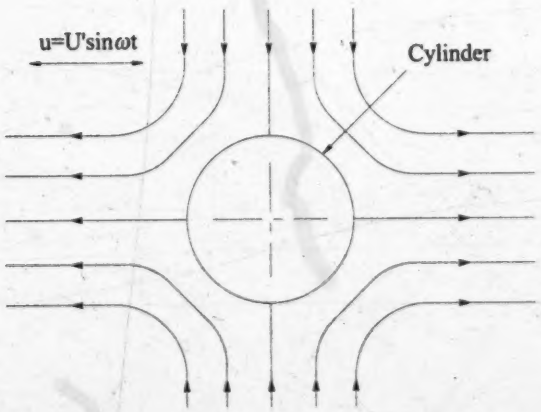

Figure 1.7: Acoustic streaming around a cylinder. The streamlines shown are the creeping flow caused by the acoustic wave perpendicular to the cylinders axis, as discussed by Lighthill (1978).

been studied in water. Davidson and Riley (1972) used hydrogen bubble flow visualization to study the jets that are created by an oscillating flow past a circular cylinder. The jets that they studied were in a direction parallel to the oscillating flow. They report that "...with an amplitude and frequency [1mm] and [45Hz] respectively, the best results were obtained ...". For these forcing parameters the Keulegan-Carpenter number would be approximately 0.3 and would correspond to a Strouhal number of approximately 3. The Reynolds number was approximately 6000. For these flow conditions they found a velocity ratio of approximately 0.035.

Williamson (1985) used flow visualization to study both a stationary cylinder in an oscillating flow field and oscillating cylinders in a stationary fluid. He examines the relationship between the forces on the cylinders and the vortices that are shed from the cylinder and the interactions between consecutive vortices. He found that the vortices that are shed from the cylinder interact with each other differently for different ranges of Keulegan-Carpenter number (KC). The regimes that he discusses are:

Pairing of attached vortices $(0 < KC < 7)$ $(\infty > St > 0.14)$

In this range Williamson (1985) reports that a pair of attached vortices are formed on each side of the cylinder as the flow moves in one direction. When the flow reverses direction these vortices pair with the newly created opposite sign vortices that are created and these two vortex pairs convect away from the cylinder. This is described as being "reasonably symmetric" for KC numbers up to approximately 4 but

for $4 < KC < 7$ the strengths of the attached vortices become unequal and "the vortex pairs do not form simultaneously upon flow reversal ...". The effect of this asymmetry on the fluid motion is not described but this asymmetry in the vortex pairs creates a force on the cylinder.

Transverse street/single pair $(7 < KC < 15)$ $(0.14 > St > 0.0\bar{6})$

This range is described as being the most repeatable. In this range there is one large vortex shed during each half cycle and the shed vortices pair rather than the attached vortices. Williamson (1985) describes a "street or 'jet' of vortices moving away from the local-flow region of the cylinder, roughly perpendicular to the oscillation direction." For the upper portion of this KC number range he describes vortices pairing and convecting away at approximately 45° from the oscillation direction.

Double pair $(15 < KC < 24)$ $(0.0\bar{6} > St > 0.041\bar{6})$

For this range of KC numbers, there are two vortices of opposite sign shed in each half cycle rather than a single vortex. These vortices pair and convect past the cylinder and away from the cylinder at some angle to the oscillation direction. Each consecutive pair will convect in the opposite direction from the previous pair.

Three pairs and four pairs -

$(24 < KC < 32)$ $(0.041\bar{6} > St > 0.0313)$ **and**

$(32 < KC < 40)$ $(0.0313 > St > 0.025)$

Williamson (1985) describes these regimes as having three and four

vortices shed in each half cycle with complex interactions between the vortices both shed from the same half cycle and from the previous half cycle. In these ranges of KC numbers, there is no mention of jets but only of pairs of vortices convecting out of the "local cylinder regions sometimes at large angles to the oscillation direction."

It appears that the most jet-like regime that was found by Williamson (1985) was for Strouhal number between approximately 0.06 and 0.14. In this region he describes the vortex street that we originally hypothesized for the SFJ. It may be that the range of Strouhal number that this type of phenomena occurs in might be different for a sharp edged flat plate than for a cylinder. The vortices will be more likely to shed in the case of a flat plate than in the case of a cylinder, because separation is a certainty.

It is also interesting to note that the direction that the vortices propagate away from the cylinder, particularly in the case of the 'pairing of attached vortices' and the 'transverse street/single pair' flow regimes, is 'roughly perpendicular to the oscillation direction'. This is the opposite of what is found with acoustic streaming around a cylinder where the mean fluid motion is parallel to the acoustic wave (see Section 1.3.2.1). It is also different than what was found by Davidson and Riley (1972) where the jets moved in a direction parallel to the oscillations.

Lipsett (1994) studied the response of a flexibly mounted rigid cylinder in an oscillatory flow. Using a U-tube apparatus the study focussed on the motion of the cylinders. The range of Keulegan-Carpenter numbers studied

were from 2 to 60 which corresponds to a Strouhal Number range of 0.017 to 0.5. No mention is made of the visualization of large scale structures or of any type of fluid jet that is produced.

1.3.2.2 Boat Bilge Keels

Another application that bears similarity to the synthetic fence jet is in boat bilge keel research. Boat bilge keels are essentially large flat plates that are below boats. One of the reasons for their existence is that they are weighted to lower the center of gravity of the boat and keep the boat from capsizing. The other purpose for bilge keels is to damp the rolling oscillations of the boat. This damping is caused by the fluid forces on the keel. For a boat that is rolling, the situation is much like a fish's tail rotating back and forth.

Sarpkaya (1986) studied the effects of damping by bilge keels through the use of a U-tube and a flat plate. He used flow visualization to study the evolution of the vortices that are shed from the edge of the plate. He found that "for [Keulegan-Carpenter numbers based on the height of the plate] less than about 3 [2] ... a newly created vortex forms a counter-rotating pair with the vortex shed in the next half cycle and convects away in a diagonal direction, either to the upper left or to the upper right of the edge of the plane." This is for a view of the plate that is much like that shown in Figure 1.1 in Section 1.2. This is similar to the findings of Williamson (1985) for cylinders in an oscillating flow in the range of Keulegan-Carpenter described as 'Pair-

[2]This corresponds to Strouhal numbers greater than about 0.3.

ing of attached vortices' or for Keulegan-Carpenter range between 0 and 7 [3]. Williamson (1985) discusses the vortices pairing and convecting away from the cylinder. For KC numbers that are lower than about 4 this is reported to be "reasonable symmetric" but less so for the upper portion of this KC range. This is discussed in more detail in Section 1.3.2.1.

Of particular interest is the fact that the range of KC numbers for which similar flow characteristics are reported are different. Adding to this is the suggestion that in order to compare these KC numbers we should be doubling the KC number based on diameter for the results given by Williamson (1985)[4]. This is because, as Sigurdson (1995) points out, the length scale that is relevant to the large scale structures for a cylinder, the diameter, is twice that for the backward facing step, the step height (or for a fence, the fence height). This is illustrated in Figure 1.8. This would mean that flow reported by Sarpkaya (1986) in the range of KC numbers from 0 to 3 is comparable to the flow reported by Williamson (1985) in the adjusted range of St numbers of 0 to 14. This suggests that similar flows occur at lower KC numbers or higher St numbers for a plate or fence than for a cylinder.

It does not appear that any jets are clearly formed in the experiments performed by Sarpkaya (1986). It may be that there were in fact jets produced but that they were not observed or reported because they were not the focus of the investigation. It may also be that the minimum value of Keulegan-

[3]This corresponds to a Strouhal number range of: $\infty > St > 0.14$

[4]or dividing the results reported by Sarpkaya (1986)

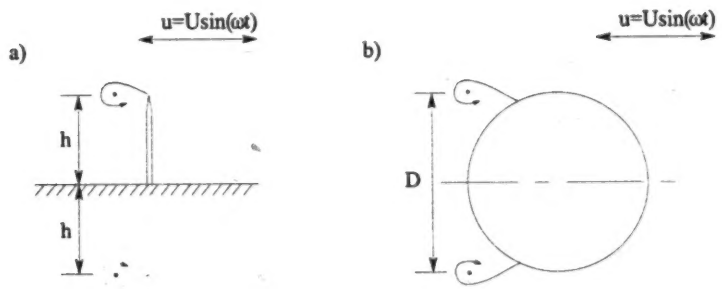

Figure 1.8: Comparison between oscillating flow past a fence and oscillating flow past a cylinder.

Carpenter number that was investigated was too high to see a clearly defined jet. The lowest value of Keulegan-Carpenter that is seen in the data in the paper is approximately 0.5. This corresponds to a Strouhal number of 2. In the current research, we study Strouhal numbers as high as 10.

1.3.2.3 Fish Tail Vortices

As discussed in Section 1.1 the synthetic fence jet is similar to a dolphin or fish flapping its tail except that instead of the tail moving it is the fluid that is moving while the 'tail' remains stationary. Another important difference between the fish tail vortex and the synthetic fence jet is that the tail undergoes some rotational motion as well as some undulatory motion. It is sensible then to look to research on the flapping fish tail for clues about the synthetic fence jet.

Ahlborn (1991) performed experiments using a flat plate that is rotated to create a "sideways flapping motion". He used aluminum filings on the water surface to visualize the starting and stopping vortices that are shed from the edges of the flat plate as it begins its rotation and stops at the end of each cycle. He studied a single flip of the tail with the associated starting and stopping vortices. In this case he found that "... a start-up eddy is produced in the first phase of the motion ... [and] as soon as the tail comes to rest, a second vortex is produced and the pair of eddies drift off parallel to the final orientation of the tail." He also studied the single flip with a return flip of the tail. In this case he found that the start-up eddy that was created with the initial flip of the tail is effectively annihilated during the return flip. He suggests that "... the destruction of the vortices ... makes the fish less detectable to predators."

Many researchers believe that the vortex structure in the wake of a swimming fish consists of a chain of vortex rings. Blickhan (1992) shows a diagram, constructed from velocities obtained by automatic particle tracking, representing the wake of a swimming fish as a chain of vortex rings. Müller (1997) used two-dimensional particle image velocimetry to study the flow pattern behind swimming mullet. The two dimensional structure that they report is consistent with a chain of vortex rings. Rayner (1995) also describes the vortex structure of the the wake behind a swimming fish as a chain of vortex rings. He also discusses the wakes behind birds in flight both gliding and flapping as well as hovering, taking-off, and even swimming. In some cases,

he suggests that the vortex structure behind some flying birds is a chain of vortex rings. In other cases he describes the structure as a series of distinct vortex rings. In the case of the swimming penguin he shows a diagram representing the vortex structure in the wake as a chain of vortex rings.

1.3.3 Conclusions From Review

Since similar phenomena exist, it is highly likely that our hypothesis is correct. It is expected that a jet can be created when a fence is introduced to an oscillating flow, provided that the non-dimensional parameters are suitably chosen. The relevant non-dimensional parameters are likely to be the Strouhal number (or the Keulegan-Carpenter number), and the Reynolds number. It is possible that the vortex structure of the jet could be a chain of vortex rings.

1.4 Specific Objectives

There were a number of goals set out at the beginning of this project. To begin with it was important to determine whether or not the hypothesis was correct. We had to show that this synthetic fence jet could actually be produced. Provided that the jet existed, we then wanted to characterize the jet. We wanted to use flow visualization to examine the vortex structure of the jet and try to better understand the mechanism that creates the jet.

In order to make the most efficient use of this new flow control mechanism, we tried to determine the optimum forcing parameters of this jet. We needed

to devise a way to measure the jet velocities in this complex three-dimensional flow for a number of different forcing parameters. This turned out to be an image correlation velocimetry (ICV) method.

1.5 Thesis Outline

This thesis is written in paper format. A bibliography is presented at the end of each chapter. The first chapter contains an introduction to the problem as well as a detailed explanation of the hypothesis and a review of the literature concerning synthetic fence jets. Chapter 2, entitled "Synthetic Fence Jets", contains a complete description of the experimental work performed on the synthetic fence jet. Chapter 3 contains the details of the image correlation velocimetry method developed to study the synthetic fence jet. Finally Chapter 4 summarizes the work of this thesis and presents conclusions as well as recommendations for future work.

BIBLIOGRAPHY

Ahlborn, B. (1991). Fish without footprints. *Journal of Theoretical Biology*, 148:521–533.

Bechert, D. and Bartenwerfer, M. (1989). The viscous flow on surfaces with longitudinal ribs. *Journal of Fluid Mechanics*, 206:105–129.

Blickhan, R. (1992). Generation of a vortex chain in the wake of a subundulatory swimmer. *Naturwissenschaften*, 79:220–221.

Bruse, M., Bechert, D., van der Hoeven, J., Hage, W., and Hoppe, G. (1993). Experiments with conventional and with novel adjustable drag - reducing surfaces. *International Conference on Near-Wall Turbulent Flows*, pages 719–738.

Choi, H., Hinze, M., and Kunisch, K. (1999). Instantaneous control of backward-facing step flows. *Applied Numerical Mathematics*, 31:133–158.

Choi, H., Moin, P., and Kim, J. (1994). Active turbulence control for drag reduction in wall-bounded flows. *Journal of Fluid Mechanics*, 262:75–110.

Choi, H., Moin, P., and Kim, J. (1998). Suboptimal control of turbulent channel flow for drag reduction. *Journal of Fluid Mechanics*, 358:245–258.

Chun, K. B. and Sung, H. J. (1996). Control of turbulent separated flow over a backward-facing step by local forcing. *Experiments in Fluids*, 21:417–426.

Chun, K. B. and Sung, H. J. (1998). Visualization of a locally-forced separated flow over a backward-facing step. *Experiments in Fluids*, 25:133–142.

Chun, S., Lee, I., and Sung, H. J. (1999). Effect of spanwise-varying local forcing on turbulent separated flow over a backward-facing step. *Experiments in Fluids*, 26:437–440.

Davidson, B. J. and Riley, N. (1972). Jets induced by oscillatory motion. *Journal of Fluid Mechanics*, 53:287–303.

Diep, J. (2001). Flow control reduction of smokestack downwash. Master's thesis, University of Alberta.

Gad-el-Hak, M. (2000). *Flow Control:passive, active, and reactive flow management.* Cambridge University Press.

Juvet, P. and Reynolds, W. (1989). Entrainment control in an acoustically controlled shrouded jet. *AIAA paper 89-0969*, pages 1–6.

Lighthill, J. (1978). Acoustic streaming. *Journal of Sound and Vibration*, 61:391–418.

Lipsett, A. W. (1994). Response of a cylinder in oscillatory flow. *Journal of Fluids and Structures*, 8:681–709.

Mallinson, S., Reizes, J., Hong, G., and Buttini, M. (1999). Synthetic jet actuators for flow control. *SPIE conference on electronics and structures for MEMS, Royal Pines Resort, Queensland, Australia*, pages 146–156.

Müller, U. K. (1997). Fish foot prints: morphology and energetics of the wake behind a continuously swimming mullet (chelon labrosus risso). *The Journal of Experimental Biology*, 200:2893–2906.

Nieuwstadt, F. T. (1998). Experiments and simulations of transition in cylindrical pipe flow. *Proceedings of the 13th Australasian Fluid Mechanics Conference*, pages 831–836.

Panton, R. (1996). *Incompressible Flow.* John Wiley & Sons, 2nd edition.

Pullin, D. and Perry, A. (1980). Some flow visualization experiments on the starting vortex. *Journal of Fluid Mechanics*, 97:239–255.

Rayner, J. (1995). Dynamics of the vortex wakes of flying and swimming vertebrates. *The Society for Experimental Biology*, pages 131–155.

Sarpkaya, T. (1986). Force on a circular cylinder in viscous oscillatory flow at low Keulegan-Carpenter numbers. *Journal of Fluid Mechanics*, 165:61–71.

Sigurdson, L. (1986). *The structure and control of a turbulent reattaching flow.* PhD thesis, Calif. Inst. Technology.

Sigurdson, L. (1995). The structure and control of a turbulent reattaching flow. *Journal of Fluid Mechanics*, 298:139–165.

Sigurdson, L. and Roshko, A. (1988). The structure and control of a turbulent reattaching flow. *Turbulence Management and Relaminarization.*

Smith, B. and Glezer, A. (1998). The formation and evolution of synthetic jets. *Physics of Fluids*, 10(9):2281–2297.

Williamson, C. H. K. (1985). Sinusoidal flow relative to circular cylinders. *Journal of Fluid Mechanics*, 155:141–174.

Zaman, K. B. M. and Hussain, F. (1980). Vortex pairing in a circular jet under controlled excitation 1:general jet response. *Journal of Fluid Mechanics*, 101:449.

Chapter 2

Synthetic Fence Jets

2.1 Introduction

An experimental study has been conducted on the jets that are created when a fence is exposed to an oscillating flow in a pipe. There has previously been research on jets created when a cylinder is placed in an oscillating flow and on the vortex structures that are created when a fence is placed in an oscillating flow. However no previous studies of jets created when a fence is introduced to an oscillating flow have been found.

Section 2.2 describes the experimental setup and apparatus used in this study. Section 2.3 contains the experimental results and discussion. Section 2.3.1 discusses the vortex structure and image correlation velocimetry (ICV) results from the experiments for the synthetic fence jet (SFJ) and Section 2.3.2 discusses the discovery and explanation of the vectored synthetic fence jet. Finally, conclusions are given in Section 2.4.

2.2 Experimental Setup and Apparatus

The pulsating pipe facility of the University of Alberta Vortex Fluid Dynamics lab (VFD lab) was developed to study pulsation induced error in orifice plate flow meters (Chapple, 1998). We decided to use this existing facility because it could be easily adapted to perform the desired experiments. This section will give a brief overview of the existing apparatus and explain in detail any modifications that were required. A detailed description of the pulsating pipe facility is given by Chapple (1998).

2.2.1 Pulsating Pipe Facility

A schematic of the pulsating pipe facility is given in Figure 2.1. This facility consists of three main parts: the pipe and blower, the pulsation system, and the data acquisition system.

The main pipe consists of 152 mm (6") schedule 80 PVC (polyvinyl chloride) pipe. At the inlet of the pipe there is a bell mouth. There is a development length of 44 pipe diameters after which there is a thin-walled clear acrylic test section. This thin-walled test section allows photography with minimal optical distortion due to the curvature of the pipe walls. At the test section, there is a joint between two sections of acrylic pipe that can be opened. There is a section of flexible pipe and a manual traverse that allow the test section to be opened for access. A blower is connected to the exit of the pipe and an axial fan or a vacuum cleaner can be connected to the outlet

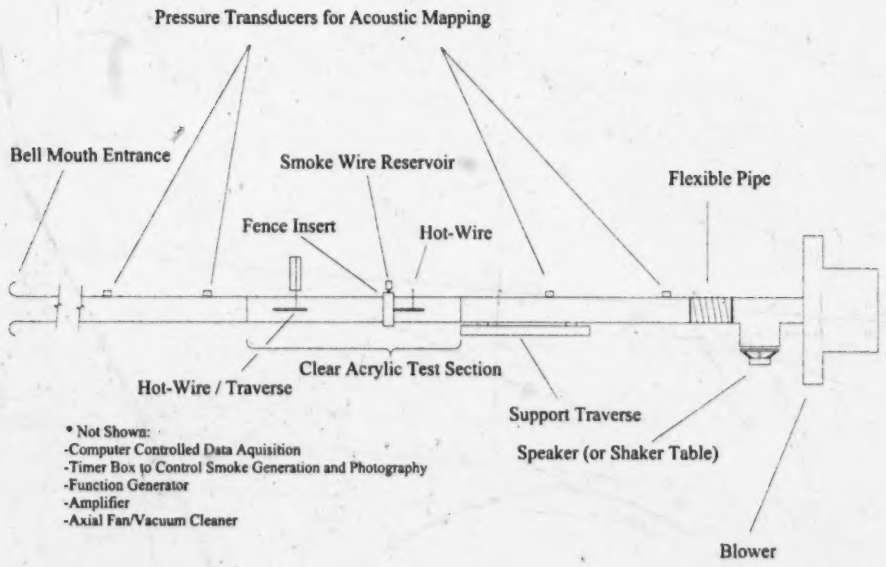

Figure 2.1: Schematic of pulsating pipe facility in the Vortex Fluid Dynamics lab at the University of Alberta

of the blower with a length of flexible duct. In the present experiment, the axial fan and the vacuum cleaner were used only to evacuate the smoke from the test section between photographs. Either the axial fan or the blower can be used to provide flow through the pipe. The axial fan has variable speed adjustability. To adjust the wind tunnel speed when the single speed blower is used, porous plates are placed at the inlet to the blower to provide a large head loss thereby controlling the flow through the pipe.

The pulsation system initially consisted of a B&K Vibration Exciter Type 4809 (shaker table) powered by an in-house built amplifier (power oscillator). This was replaced for the final experiments by a 203 mm (8") subwoofer powered by a Pioneer® stereo receiver model number SX-3600 (amplifier). The sine wave signal to the amplifier (or power oscillator) was provided by a B&K precision 3030 Sweep/Function Generator. For non-sinusoidal forcing, the desired waveform was created using Matlab® and the signal was output through the computer's Sound Blaster® Live! Value 16 bit sound card. The speaker (or vibration exciter) is connected to the pipe via a T-intersection as seen in Figure 2.1. This allows independent pulsation and flow rate through the pipe.

Throughout the pipe are a number of sensors that collect various data. There are four validyne pressure transducers along the length of the pipe that measure the pressure in the pipe. The signals from both of these pairs of pressure transducers are used to estimate the acoustic pressure and velocity distribution along the pipe. Each pair, along with acoustic equations, can be

used to couple the measured pressure fluctuations with the expected velocity fluctuations. This was achieved using a LabVIEW® program that was previously written for the orifice plate flow meter experiments (Chapple, 1998). In the present research, the amplitude of the velocity oscillations at the fence location were estimated using this program. Two additional pressure transducers are located at the test section on either side of the fence insert. There are two hot-wire anemometers in the pipe. One is located in the test section and the other is located upstream of the test section. The hot-wire located upstream of the test section is mounted on a computer controlled traverse that allows the flow rate in the pipe to be measured by obtaining a velocity profile across the pipe. The output from each of these sensors are connected to a data acquisition system. The data acquisition and analysis are provided by a 12-bit AT-MIO-16-E10 National Instruments® data acquisition board in an 800 MHz Pentium® computer[1] using LabVIEW® 4.0.1.

2.2.2 Smoke Wire Flow Visualization

Flow visualization was done using a smoke-wire. This method was developed by Chapple (1998) with information from Corke et al. (1977). The method involves allowing a drop of oil to fall along a very small diameter wire (0.127 mm or 0.005"). As the drop falls it leaves small beads of oil along the length of the wire at approximately regular intervals. An electric current is then passed through the wire. The resistance of the wire causes it to

[1]preliminary testing was performed using a 166 Mhz Pentium® with the same data acquisition board and software

heat up generating smoke at each bead of oil. When using this technique it is important to consider the effects of buoyancy. Because we are relying on heat to generate the smoke, we are also creating some buoyancy. When choosing the orientation of the fence we carefully considered the possible effects of buoyancy. Also, when looking at the photographs we were careful to consider the possible effects of buoyancy.

2.2.3 Timing Box and Photography

Photographs were taken with a Nikon® F3 35mm camera. High speed TMAX Kodak® P3200 ASA black and white print film was used for black and white photographs For colour photographs Kodak P1600 Ektachrome colour slide film was used and the film was push-processed to 3200.

Illumination was provided by either one or two General Radio® Type 1540 Strobolume stroboscopes. Two stroboscopes were used for image correlation velocimetry photographs as described in Chapter 3. These stroboscopes have a very short duration flash ($\sim 25\mu s$).

A sophisticated in-house built electronic timing box was used to control the timing of all photography elements. The timing box is capable of activating 10 different devices. It has a resolution of 1 μs. This allows very precise control of the timed elements. The timing box controlled the sequence of events listed in Table 2.1.

Table 2.1: Sequence of events controlled by the electronic timing box

1	Turn off room lighting (a table lamp)
2	Turn on smoke wire
3	Open camera shutter (* or fire the camera)
4	Fire first stroboscope *
5	Fire second stroboscope *(if applicable)
6	Close camera shutter *
7	Turn off smoke wire
8	Turn on room lighting
	* in some cases a single strobe was fired by the camera and the camera was set to 1/60 second exposure

2.2.4 Fence Insert

In order to use the pulsating pipe facility for researching SFJs, fences needed to be made to fit with the existing apparatus. Throughout the current research, three fence designs were used. In order to prove the existence of the SFJ, we made a simple fence insert that worked with the existing pulsating pipe facility. After it was proven that the SFJ could be created, an intermediate design was constructed. The final design was created based on what was learned from the first two designs.

The preliminary design was made to use an existing joiner alignment ring that housed the orifice plate from the previous experiments in the pulsating pipe facility. The fence was made to fit between the two sections of clear acrylic pipe that make up the test section. O-rings were used between the pipe and the fence insert on both sides to provide a seal. The fence was made from 3.2 mm (1/8") thick lexan® . The fence's edge is a straight line

forming a chord of the circular cross-section of the pipe. It was made to be approximately 25.4 mm (1") in height at the middle of the fence where the height is a maximum. The edge of the fence was sanded to form a sharp edge. The fence could be oriented so that it protruded into the pipe from the bottom, top or side of the pipe. The best results were obtained with the fence protruding into the pipe from the side of the pipe wall. A rendering of the preliminary fence is shown in Figure 2.2.

The second design was constructed to allow fences with different heights to be inserted without opening the test section. A new joint alignment ring was made from PVC pipe. A slot was cut into the side of the ring for a fence to slide into. The fence was held in place with screws. Two fences were made: a 25.4 mm (1") height fence and a 12.7 mm (1/2") height fence. The edges of these fences were chamfered at 60° to create a sharp edge. It was discovered that the jet would bifurcate at lower values of U' which was due to the existence of the secondary edges. For the final fence insert design we used a knife edge in order to eliminate this effect, however interesting it was. The edge designs used for the intermediate fence and the final fence are shown in Figure 2.4

The final design was similar to the second design with a few modifications. The fences as well as the new joint alignment ring were constructed of steel. As with the second design, a slot cut into the side of the ring allows the fences to be inserted without opening the test section. Assembly drawings of the ring are shown in Figures 2.5 and 2.6. Three pressure ports were placed

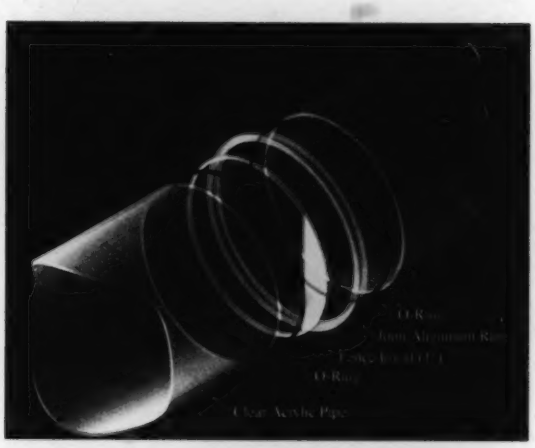

Figure 2.2: Rendering of preliminary fence insert assembly: unassembled. The pipe is separated as in the opened position. O-rings are placed on each side of the fence to provide an air-tight seal.

Figure 2.3: Rendering of preliminary fence insert assembly: assembled.

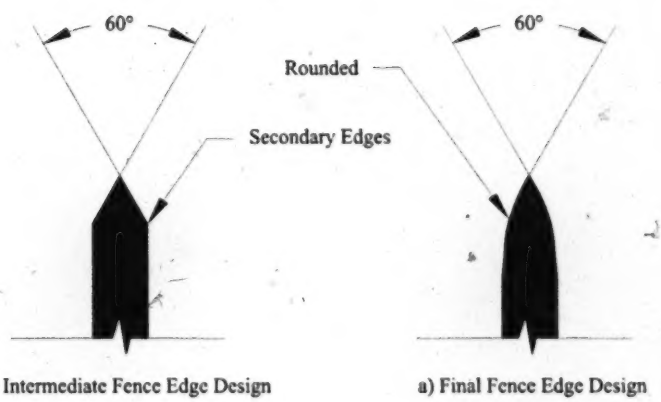

Figure 2.4: Intermediate and final fence edge design. a) Shows the intermediate fence edge design. A simple chamfer of 60° to produce small secondary edges. b) Shows the final fence edge design. The edge is chamfered as in a) then the edges are rounded to produce a knife edge with only one edge.

on each side of the fence in order to measure the pressure variation across the fence. One pressure port was centered on the fence and two were placed 30° away from the middle. These were included as a possible diagnostic tool to better understand the vectored synthetic fence jet(see Section 2.3.2).

2.2.5 Resonance Map of Pipe

One of the limitations of the pulsating pipe facility ~~is that~~ it is effectively a large organ pipe. As a result of this, it has certain resonant frequencies at which the amplitude of the standing wave is amplified and other frequencies at which the standing wave is damped. Also, since the location of the test section is fixed, there are frequencies at which the velocity nodes are coincident with the fence location. At these frequencies there will be no unsteady flow past the fence, therefore there can not be an SFJ. At other frequencies there will be a velocity antinode at the fence location. At these frequencies a wider range in the velocity amplitude at the fence can be achieved.

To determine which frequencies were resonances of the experimental apparatus we produced a resonance map of the pipe and excitation system. The forcing frequency was varied while maintaining a constant amplitude setting on both the amplifier and the function generator. The maximum velocity amplitude (U'_{max}) in the pipe and the velocity amplitude at the fence location (U'_{fence}) were recorded and plotted against frequency. The resulting plots are shown in Figure 2.7. The local maxima and minima of these plot are tabulated in Tables 2.2 and 2.3. These values gave an indication of what

Figure 2.5: Rendering of final fence insert assembly. Both the 25.4 mm (1") fence and the 12.7 mm (1/2") fence are shown. The pipe is separated as in the opened position. Screws (not shown) hold the fence in place.

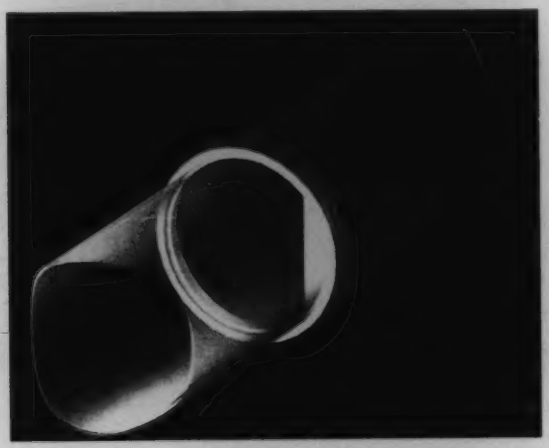

Figure 2.6: Rendering of final fence insert assembly: Assembled. The pipe is closed. Screws through the slit in the joint alignment ring hold the fence in place.

frequencies we could achieve the largest velocity amplitudes in the pipe as well as at the fence. Throughout the experiments, the porous plate labelled '1 m/s' was in place at the inlet to the blower. If the plate were removed or a different plate added then the pipes end condition would be changed and a new resonance map would be required.

Table 2.2: Maxima And Minima Of Resonance Map For U'_{max}

Maxima Frequency (Hz)	U'_{max} (cm/s)	Minima Frequency (Hz)	U'_{max} (cm/s)
13	28	17-20	7
27	32	32-37	10
41	27	48	7
54	22	67	8
69	12	73-77	3
82	20	84	14
86	27	87-90	6
96	20	100	7

Table 2.3: Maxima And Minima Of Resonance Map For U'_{fence}

Maxima Frequency (Hz)	U'_{fence} (cm/s)	Frequency (Hz)	Minima U'_{fence} (cm/s)
13	12	18	6
27	17	31	1
41	7	50	1
55-62	11-12	72	0
82	19	92	1
96	10	100	6

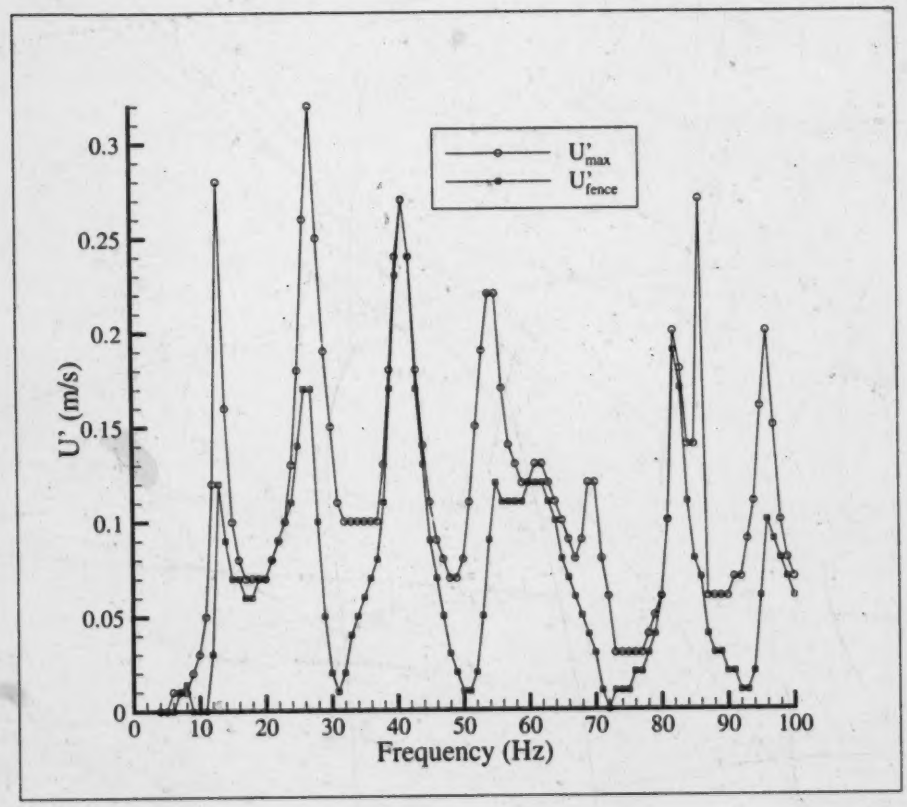

Figure 2.7: Resonance map of pulsating pipe facility. U'_{fence} is the amplitude of the fluctuating velocity at the fence location. U'_{max} is the amplitude of the maximum fluctuating velocity in the pipe (location independent).

2.3 Results and Discussion

There are two main sections that will be discussed: Synthetic Fence Jet and Vectored Synthetic Fence Jet. The Synthetic Fence Jet section will begin with a description of the 'search' for the SFJ and an outline of the parameters for which jetting occurred followed by the ICV results for the SFJ and finally a discussion about the structure of the SFJ will be presented. The Vectored Synthetic Fence Jet section will explain what the vectored synthetic fence jet is and explain the phenomenon.

2.3.1 Synthetic Fence Jet

Here we will present the 'search' for the SFJ followed by the ICV results for the SFJ and the details of the flow structure.

2.3.1.1 "Search" For Synthetic Fence Jet

Using the smoke wire flow visualization method described in Section 2.2.2 and a single stroboscope to illuminate a sheet in the test section and varying both the amplitude (U'_{fence}) and the frequency (f_{ex}) of the velocity fluctuation we were able to see whether or not a jet was created. As was expected, a jet was created at the frequencies corresponding to the maxima in the resonance map for U'_{fence}. The jets could be found at these frequencies not because jets can only be created at these frequencies but because, in the pulsating pipe facility, the amplitude at the fence location can be made sufficiently high to

create a jet at these frequencies.

During the initial 'search' for jets the power oscillator and shaker table were used to produce the oscillating flow in the pipe. There were some inconsistencies in the parameters that would produce a jet. It was noted by John Diep who was using the same power oscillator for his experiments that the tone generated was different from day to day. It turned out that these results were due to the power oscillator. The output from the power oscillator was not sinusoidal. This led to the discovery of the vectored synthetic fence jet (VSFJ). This phenomenon is discussed in detail in Section 2.3.2. The shaker table and power oscillator were replaced by the subwoofer and audio amplifier for further experiments and the output from the audio amplifier was verified as being sinusoidal (when the input was sinusoidal).

Using the subwoofer and audio amplifier a detailed map of what ranges of frequency and velocity amplitude at the fence a jet can be created was constructed. At frequencies that a jet is produced, it is clear from the flow visualization that as the forcing amplitude is reduced there is a slow decay of the strength of the jet from where the jet appears to be uninfluenced by the buoyancy of the smoke to where the buoyancy of the smoke dominates the flow. As the forcing amplitude is increased, the signal reported by the pressure transducers in the pipe begin to distort and become non-sinusoidal. This is due to the limitations of the amplifier or the speaker. In mapping the range we used the point at which there is still sufficient strength in the jet to be visible, but where the buoyancy is clearly becoming dominant as

the minimum of the range and the point when the signal at the pressure transducers in the pipe show a first harmonic of approximately 10% for the maximum amplitude. The map of parameters for which jetting occurs is tabulated for the 25.4 mm (1") fence in Table 2.4 and for the 12.7 mm (1/2") fence in Table 2.5.

Table 2.4: Map Of Parameters For Which Jetting Occurs For 25.4 mm (1") Fence

Frequency (Hz)	U'fence (m/s) lower	upper	St upper	lower	Re lower	upper
41	0.22	1.20	4.7	0.9	358	1954
45	0.22	0.30	5.2	3.8	358	488
35	0.23	0.30	3.9	3.0	374	488
12	0.8	0.8	3.8	3.8	130	130
27	0.20	0.75	3.4	0.9	326	1221
24	0.20	0.40	3.1	1.5	326	651
20	0.20	0.30	2.5	1.7	326	488
55	0.30	0.40	4.7	3.5	488	651
62	0.22	0.30	7.2	5.3	358	488
83	0.30	0.50	7.0	4.2	488	814
96	0.24	0.24	10.2	10.2	391	391

2.3.1.2 The Plan

As described in Section 1.4 we wanted to characterize the SFJ and determine the optimum forcing parameters.

To begin with we did a series of experiments to attempt to learn as much as possible about the large scale vortex structures that make up the SFJ. Using preliminary black and white photographs as well as the colour ICV

Table 2.5: Map Of Parameters For Which Jetting Occurs For 12.7 mm (1/2") Fence

Frequency (Hz)	U'fence (m/s) lower	upper	St upper	lower	Re lower	upper
41	0.40	1.20	1.3	0.4	326	977
45	0.30	0.30	1.9	1.9	244	244
12 *	0.8	0.8	1.9	1.9	65	65
27	0.35	0.75	1.0	0.5	285	611
24	0.30	0.40	1.0	0.8	244	326
55	0.30	0.40	2.3	1.8	244	326
62	0.30	0.30	2.6	2.6	244	244
83	0.44	0.44	2.4	2.4	358	358
96 *	0.25	0.25	4.9	4.9	204	204

*note: Jetting was extremely weak at these frequencies

photographs and ICV results we wanted to develop some theories as to the structure of the SFJ. As discussed in Section 1.2.5, the Strouhal number is expected to be the most important non-dimensional parameter. This is supported by the findings of the literature survey as other researchers found that the Keulegan-Carpenter number (the inverse of the St) is an important parameter. In order to determine the effect of the Strouhal number on the jet strength we wanted to keep Re constant and vary only the Strouhal number and see how the velocity ratio (u_j/U'_{fence}) varies. In order to accomplish this we needed to carefully examine the ranges in which we could actually produce the jet. Also, we needed to be able to measure the jet velocity with some confidence. We used the image correlation velocimetry method detailed in Chapter 3.

The experimental plan of which types of experiments to try involved using

the ICV method on the parameters as follows:

1. (a) Keep Re constant and vary St (by varying frequency, amplitude and fence height)

   (b) Keep Re and St constant

   (c) Keep U'_{fence} constant (different Re for different fence heights)

2. Repeat 1. above for a different U'_{fence}

3. Vary $U'_{fence}$for a single frequency

4. Keep St constant and vary U'_{fence}

Due to the limited range of forcing parameters at which a jet can be produced it was difficult to achieve a large number of data points for some parts of this experimental plan. We were able to obtain a reasonable amount of data for parts 1a) and 2a) as well as a few data points for part 3.

2.3.1.3 Image Correlation Velocimetry Results

This section discusses the ICV experiments that were performed on the SFJ and details the results.

In order to characterize the SFJ we required some measure of its strength. The simplest measure of a jet's strength is its velocity at some fixed position. We decided to use the velocity of the jet at the center of the pipe. Measuring the velocity is particularly difficult because the flow is completely

three dimensional and has a fully reversing component. Hot-wire anemometers are unable to distinguish flow direction and are therefore unsuitable. We elected to use ICV to measure the jet velocities. Chapter 3 contains a complete description of the ICV method that we adapted from Papamoschou and Bunyajitradulya (1997) along with an explanation of some of the experiments that were performed using the technique. The pipe centerline is the easiest position to locate because it is readily identified by the grid that was used (see Section 3.4.2.2). Also, it is the point which has the minimum optical distortion due to the curvature of the pipe. Finally, it is the furthest from any stationary objects, such as the pipe walls, that could interfere with the ICV's ability to work correctly.

The experiments involved taking five ICV photographs for each forcing condition. In some cases, one or two photographs did not turn out so there were only three or four photographs. The forcing conditions used were determined by looking at the map of the parameters for which jetting occurs (see Tables 2.5 and 2.4 in Section 2.3.1.1) and figuring out how to achieve the most data points that are a part of the experimental plan (see Section 2.3.1.2). The results from each set of five photographs were then averaged. In averaging the photographs, zero velocities were not included in the average because the ICV program outputs a zero velocity for points at which the velocity is not calculated due to insufficient image data.

Figure 2.8 shows an ICV photograph of the SFJ. The fence height was 25.4 mm (1") and the forcing frequency and amplitude were 24 Hz and 0.38

m/s respectively. The Strouhal number was 1.6 and the Reynolds number was 620 for these forcing conditions. The jet is clearly confined to near the middle of the fence. Near the top and, to a lesser degree, near the bottom of the smoke wire the smoke has moved to the left indicating that the flow is recirculating in the plane of the fence. This is supported by the ICV result given in Figure 2.9. The vectors represent the calculated jet velocity and the image represents the smoke. The area shown is only in the middle of the pipe, vertically to a radius of approximately 30 mm and horizontally to a radius of approximately 50 mm. The radius of the pipe is approximately 76 mm. Where there is smoke to visualize the flow, the vectors show a recirculation in the upper and lower half of the pipe. The averaged ICV result along with the individual ICV results for the set of five photographs that include Figure 2.9 is shown in Figure 2.10. The averaged streamlines look right. They average out to a horizontal jet flow in the middle. They show some vortex structure. The vectors are reasonably smooth and continuous and are pointed in the direction that the jet moves. The recirculation is also visible in the averaged velocity field.

We took the average velocity of the jet at the center of the pipe to represent the jet velocity. The ICV results seen in Figure 2.11 show that there are larger measured fluctuations in the 5 photograph averaged velocity for a Strouhal number of 1.6 and for a Reynolds number of 620. These fluctuations are due to the high turbulence intensity expected in this highly forced unsteady flow combined with an insufficient number of photographs to de-

Figure 2.8: ICV photograph of SFJ. Parameters: h=25.4 mm (1"), $f_{ex} = 24$ Hz, U'_{fence}= 0.38m/s, St=1.6, Re=620.

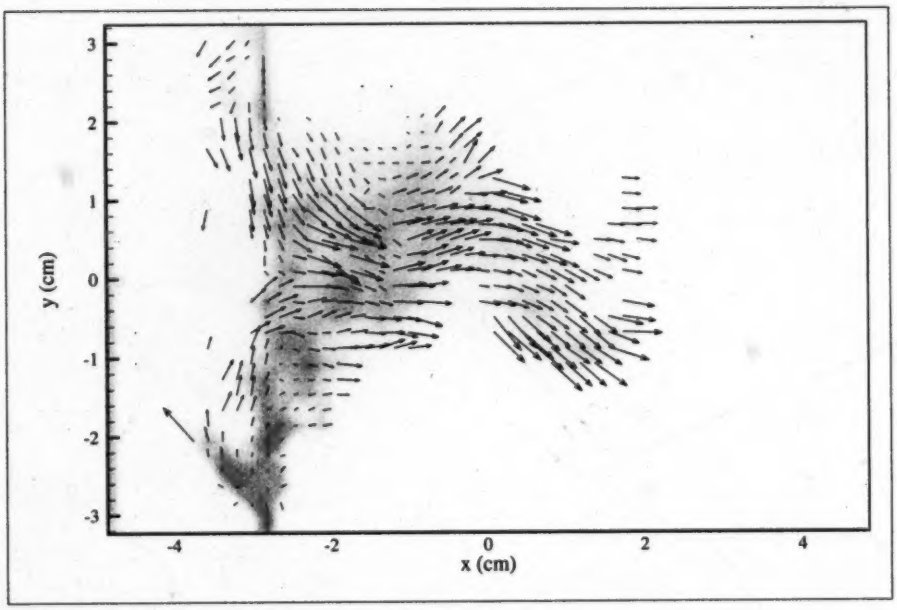

Figure 2.9: ICV result from photograph shown in figure 2.8. Parameters: h=25.4 mm (1"), f_{ex} = 24 Hz, U'_{fence}= 0.38m/s, St=1.6, Re=620.

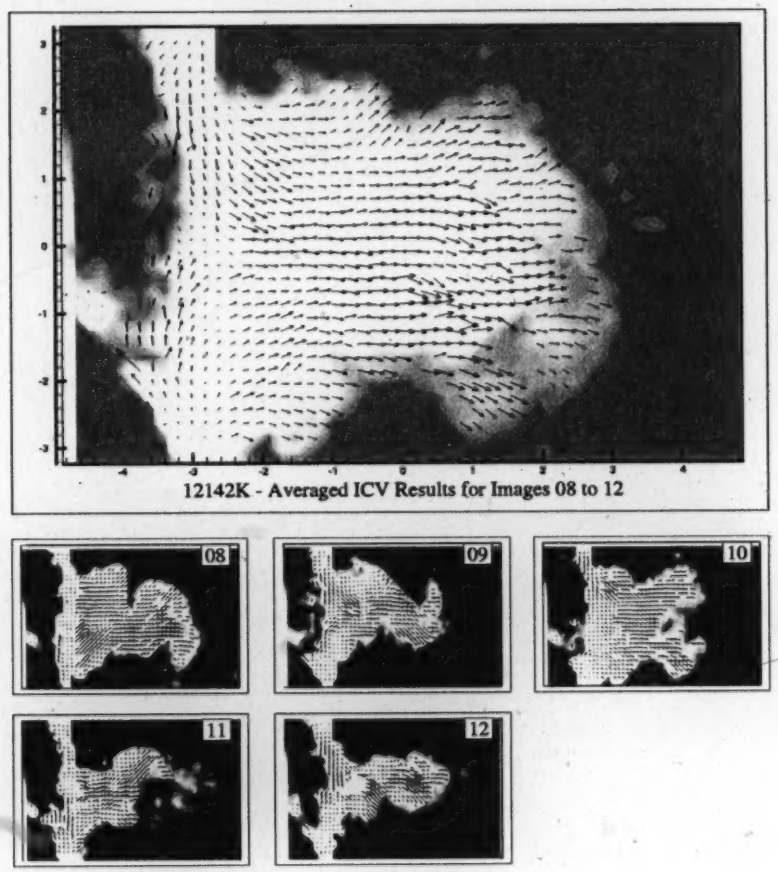

Figure 2.10: Set of ICV results with averaged ICV result. Parameters: h=25.4 mm (1"), f_{ex} = 24 Hz, U'_{fence}= 0.38m/s, St=1.6, Re=620.

termine an actual steady average. For higher Strouhal numbers the scatter in the calculated velocity fluctuation is significantly reduced. The maximum velocity ratio (U_j/U'_{fence}) for a Reynolds number of 620 was found to be approximately 0.94 at a Strouhal number of 1.6. The minimum velocity ratio was found to be approximately 0.14 at a Strouhal number of 0.68. The maximum velocity ratio averaged for all the data at each Strouhal number for a Reynolds number of 620 was found to be 0.55 at a Strouhal number of 1.8.

The velocity ratios for the 12.5 mm (1/2") fence were considerably lower than for the 25.4 mm (1") fence. This was the case for all of the data. The maximum velocity ratio found with the 12.5 mm (1/2") fence was 0.17. Figure 2.12 shows the same plot for a Reynolds number of 410. This figure shows an increase in velocity ratio as the Strouhal number is decreased for the 25.4 mm (1") fence.

Figure 2.13 shows a plot of velocity ratio against Reynolds number for a constant frequency of 40 Hz. This was obtained by increasing the amplitude and maintaining a constant frequency of 40 Hz and fence height of 25.4 mm (1"). There is clearly a reduction in velocity ratio with increasing Reynolds number. This particular set of data is very limited and it is very difficult to draw any firm conclusions. However, this curve suggests that the jet is more efficient at lower Reynolds numbers or at lower amplitudes of velocity fluctuation. In order to determine which, we would have to vary both fence height (h) and the kinematic viscosity of the working fluid (ν) along with the forcing amplitude.

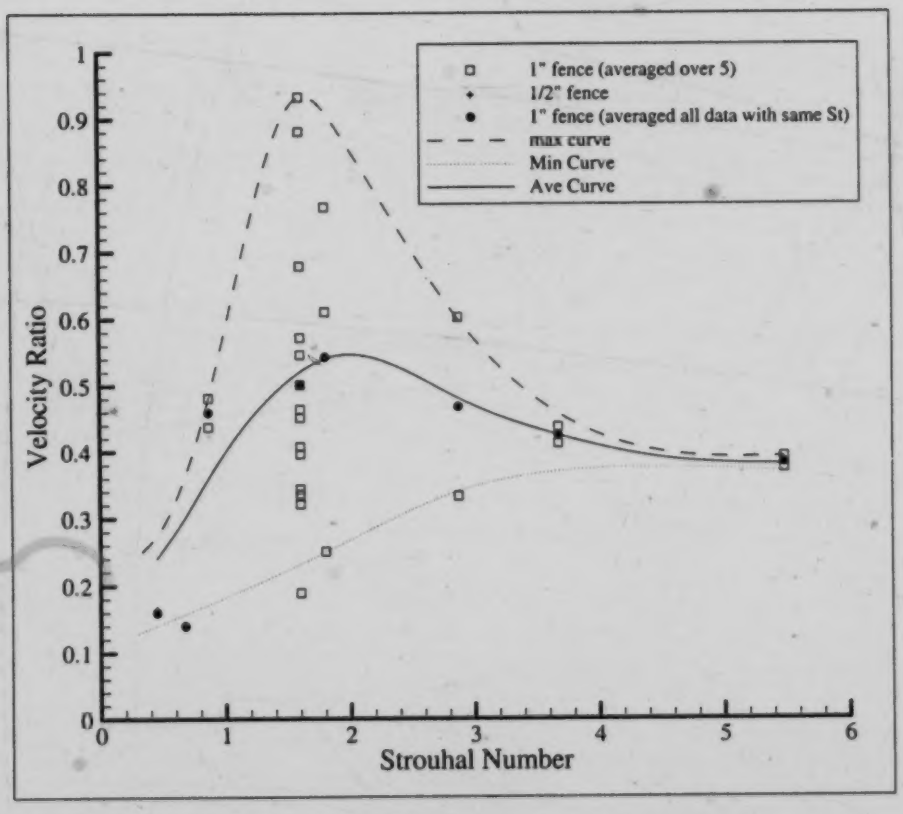

Figure 2.11: Plot of velocity ratio against Strouhal number for Re=620. Includes data from the 25.4 mm (1") fence and the 12.7 mm (1/2") fence. Data averaged over 5 is data from each set of 5 photographs taken. Data averaged over all data with same Strouhal number includes data from separate experiments with the same Strouhal number.

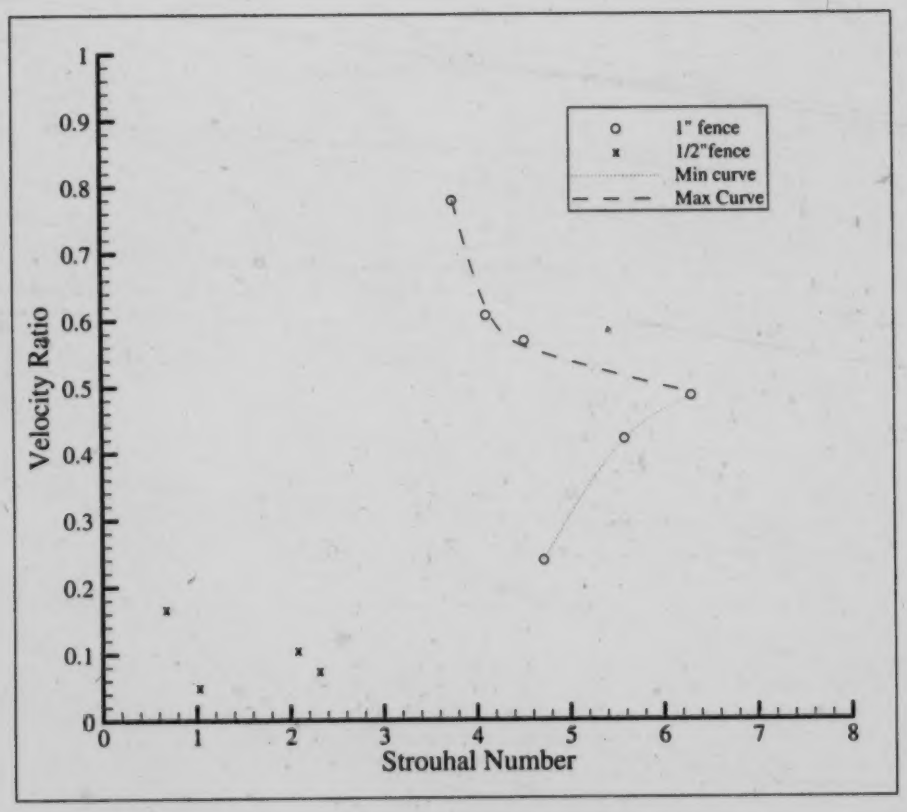

Figure 2.12: Plot of velocity ratio against Strouhal number for Re=410.

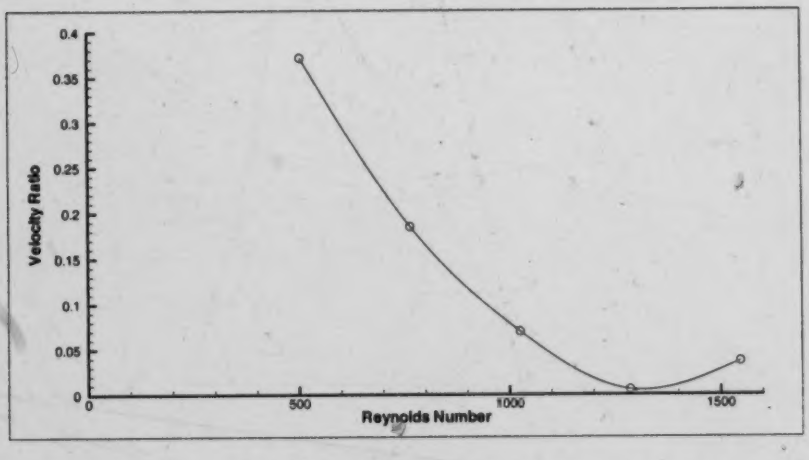

Figure 2.13: Plot of velocity ratio against Reynolds number for constant frequency of 40 Hz.

2.3.1.4 Vortex Structure

In Section 1.2 we describe the theoretical basis for the hypothesis that a jet can be created at the edge of a fence in an oscillating flow. This theory is discussing a 2D flow in the sense of being uniform along the length of the fence. Because of the experimental setup used, the flow is not expected to be 2D. Experiments were performed in a round pipe. If a rectangular pipe were used instead of the round pipe, the flow might be more two-dimensional. The presence of the round pipe means that the fence height varies along its length which contributes to the three-dimensionality of the flow. The jet only appears at the middle of the fence. The jet may amplify better at a certain fence height, but then we would expect jets on the sides of the fence

at times. This was not observed. The jet location is more likely due to the recirculating nature of the flow due to the pipe boundary. However it could just as easily recirculate along the pipe axis instead, which it probably does.

As seen in Section 1.3.2 there is strong evidence to support the idea that the flow structure in the wake of a swimming fish is a chain of vortex rings. Due to the similarities between the swimming fish and the SFJ it is reasonable to expect a similar flow structure for the SFJ. One difference, of course, is that the wake of a steadily swimming fish should actually be momentumless as it is for any self-propelled non-accelerating body.

For some of the higher Strouhal number cases it appears that there is a staggered arrangement of vortices as was suggested as the basic mechanism of jet production and is illustrated in Figure 1.4(h) on Page 11. This arrangement of vortices is the same as a 2D slice of a chain of vortex rings as described by Sigurdson (1986), seen in Figure 2.14(c). We would expect to see this arrangement of vortices in the SFJ when looking at the flow in a direction aligned with the sharp edge of the fence, however at a Reynolds number of 358 we see it when looking in an orthogonal direction along the axis of the pipe as seen in Figures 2.15 and 2.16. It is possible that the chain of vortex rings has twisted to present this view, or has evolved in a different manner than suggested in Figure 1.4(h). At higher Reynolds numbers the smoke is dissipated more quickly and the structure is not easily determined.

Chen (2001) performed some two-dimensional direct numerical simulations of the SFJ and found that the frequency of the large scale structures

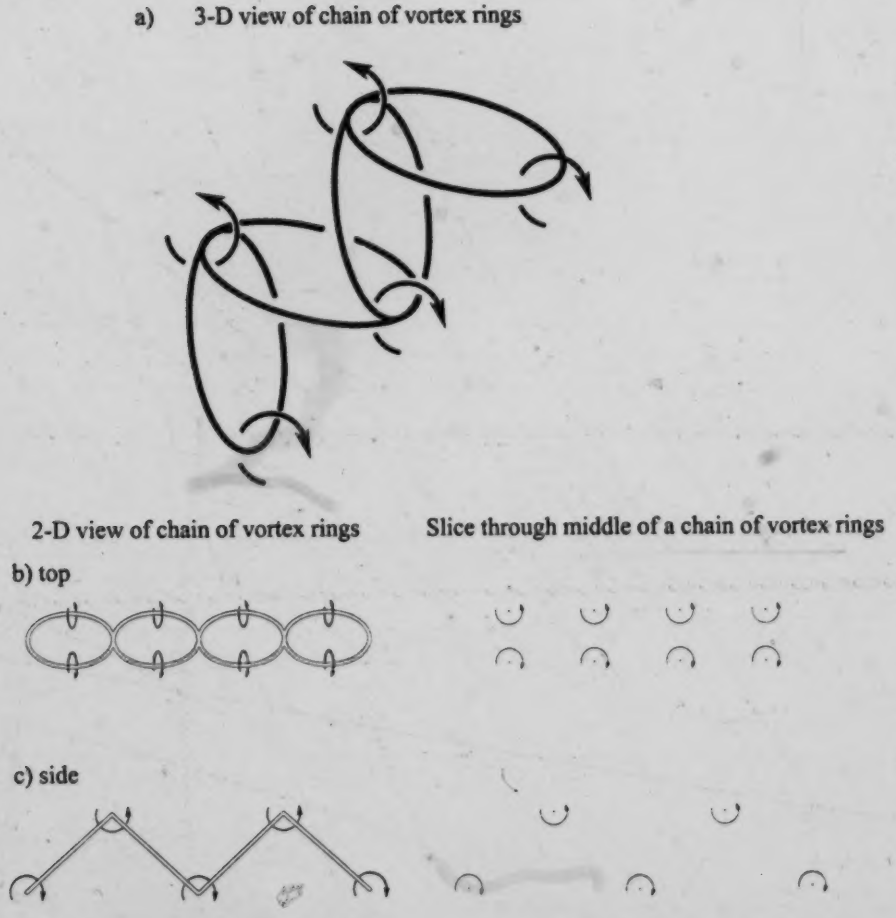
a) 3-D view of chain of vortex rings
2-D view of chain of vortex rings
Slice through middle of a chain of vortex rings
b) top
c) side

Figure 2.14: Chain of vortex rings. A 3-dimensional chain of vortex rings appear as a set of vortices side by side, as in (b), or a staggered set of vortices, as in (c), depending on which axis is sliced along. Adapted from Sigurdson (1986)

Figure 2.15: Photograph of SFJ suggesting chain of vortex rings. Parameters: h=25.4 mm (1"), f_{ex} = 42 Hz, U'_{fence}= 0.22m/s, St=4.96, Re=358.

Figure 2.16: Photograph of SFJ suggesting chain of vortex rings. Parameters: h=25.4 mm (1"), f_{ex} = 41.1 Hz, U'_{fence}= 0.20m/s, St=5.14, Re=326.

Figure 2.17: Schematic of frequency calculation. u_c is the convection velocity of the vorticies. u_j is the centerline jet velocity. λ is the wavelength. Γ is the circulation. f_v is the frequency of the vorticies.

was approximately $1/7^{th}$ of the forcing frequency. He saw an initially laminar jet which underwent an instability at the lower frequency. In order to compare this result with the experimental result we estimated the frequency of the large scale structures in Figure 2.16. The frequency can be obtained from the convection velocity of the vortices and the distance between vortices as seen in Figure 2.17.

The jet velocity for this case was approximated by using the velocity ratio from an ICV result and assuming that it was the same for this case. We guessed a velocity ratio of 0.7 which is among the highest velocity ratios that were found. The frequency of the large scale structures was found to be approximately $1/20^{th}$ of the forcing frequency. The difference between this result and the numerical result of Chen (2001) could be because of the approximations we made and because the numerical simulation was unbounded and two-dimensional while the experiment was bounded by the pipe and fully

three-dimensional.

If the jet creation mechanism was the shedding of the vortices at the forcing frequency then we would expect the frequency of the vortex structures to be the same as the forcing frequency. The difference between the forcing frequency and the frequency of the large scale vortex structures could be explained either by approximately 4 pairings of the created vortices or by an initially laminar jet developing the lower frequency instability. Each pairing would reduce the frequency by half so that by the 4^{th} pairing the frequency would be $1/16^{th}$ of the forcing frequency. In Figure 2.16 the large scale vortex structures are seen in the middle of the pipe and not near to the fence. This supports the suggestion that the jet is initially laminar and develops a lower frequency instability. It is likely that the basic mechanism of jet production is more complex than was hypothesized as illustrated in Figure 1.4 on Page 11.

2.3.2 Vectored Synthetic Fence Jet

Here we will explain what the vectored synthetic fence jet is, how it was discovered, and the mechanism that causes this phenomenon. We discovered that the synthetic fence jet could be vectored by altering the forcing waveform. This occurred during the preliminary testing of the synthetic fence jet when using the shaker table as an acoustic actuator. Figure 2.18 shows that the jet was vectored at an angle of approximately 45 degrees for this particular situation. We also found that the direction of the vectoring could be reversed by reversing the leads to the shaker table. In order to verify

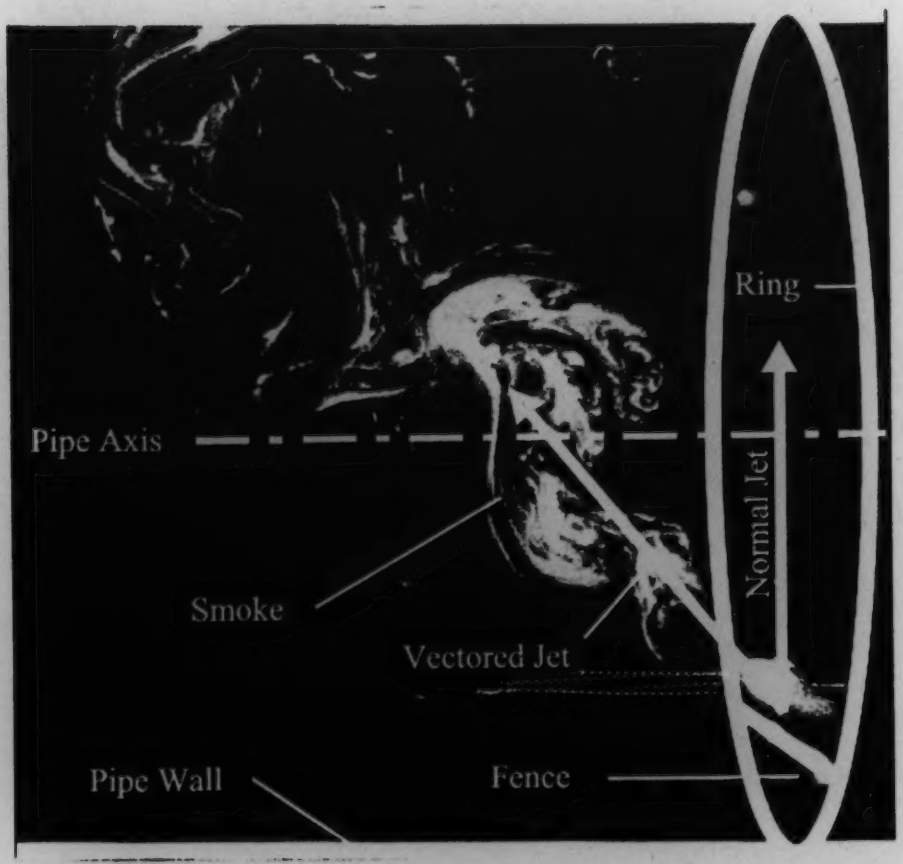

Figure 2.18: Bottom view of vectored synthetic fence jet. Arrows show the usual jet direction normal to the pipe wall and approximate actual jet direction. Fence, fence ring and pipe walls have been highlighted in white and the centerline of pipe is represented by the dashed line. Parameters: h=25.4 mm (1"), f_{ex} = 60.25 Hz, U'_{fence}= 0.43m/s, St=3.6, Re=700.

that the vectoring was not caused by a mean flow through the pipe, a plug was placed in the end of the pipe effectively eliminating any possible mean flow. The vectoring of the jet remained. After searching for a cause of this anomalous vectoring behavior, it turned out that the power oscillator being used was damaged resulting in a non-sinusoidal output. The signal produced by the power oscillator is shown in Figure 2.19.

The resulting pressure transducer signal at one location of the pipe is shown in Figure 2.20. This signal indicates that the non-sinusoidal signal generated by the power oscillator propagates into the acoustic wave in the pipe.

With the fence removed a hot-wire was positioned near the fence location and the signal was recorded. It is shown in Figure 2.21. This was used only as a relative measure of velocity to get a better indication of what the flow at the fence was. Since hot-wire anemometers are unable to distinguish flow direction and the flow is reversing, we are unable to ascertain which portions of the signal correspond to flow in the positive direction and which portions correspond to flow in the negative direction. It seems clear that the flow is in one direction for the high, narrow peak and in the other for the lower, wider double peak. By studying the characteristics of these signals we were able to develop a theory to explain the vectoring of the jet.

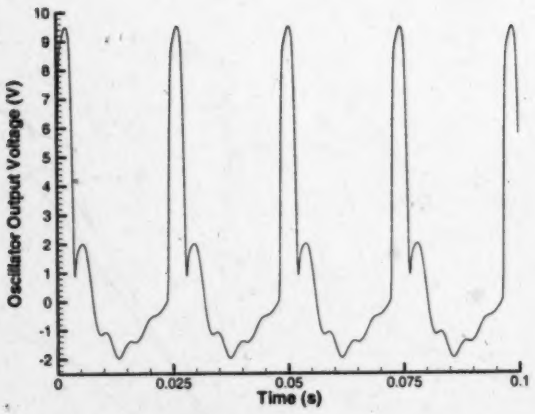

Figure 2.19: Voltage signal produced by the damaged power oscillator. Input to the power oscillator is a sine wave.

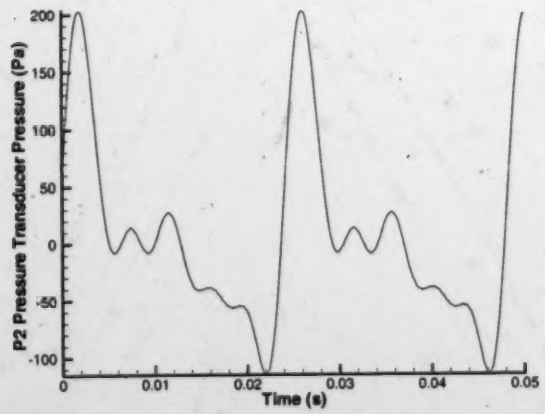

Figure 2.20: Pressure at transducer P2 in the pipe due to non-sinusoidal forcing of damaged power oscillator. The acoustic wave in the pipe is non-sinusoidal

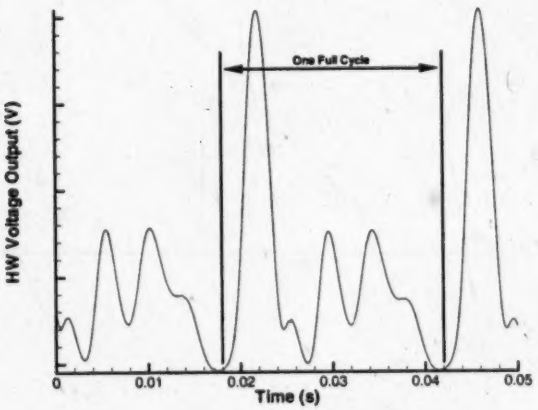

Figure 2.21: Hot-wire voltage trace at fence location with fence removed. Forcing by non-sinusoidal damaged power oscillator.

2.3.2.1 Proposed Mechanism

We present here the details of a proposed mechanism by which the jet is vectored that is based on the Biot-Savart law of vortex dynamics. This mechanism was developed based on an analysis of hot-wire measurements of the acoustic wave, vortex dynamics theory, and analysis of photographs. The basic concept of the proposed mechanism is that there is an inequality in the amounts of positive and negative vorticity generated. We will consider the highly idealized case of only two vortices, which represent only one cycle of the oscillating acoustic velocity. If more vorticity is generated during the flow in one direction than is generated during the flow in the other direction then 2-D point vortex theory suggests that the vortices will curve in a circular

path to the side that has the stronger vortex. This is depicted in Figure 2.22. The effect is caused by the difference in the induced velocities between the two vortices. As seen in Figure 2.22(a) the velocity of the weaker vortex, v_B, induced by the stronger vortex is greater than the velocity of the stronger vortex, v_A, induced by the weaker vortex. This causes the weaker vortex to move ahead of, and towards the side of, the stronger vortex resulting in the curved path shown in Figure 2.22(b). In this example, vortex A is a factor of n times as strong as vortex B, and of opposite sign.

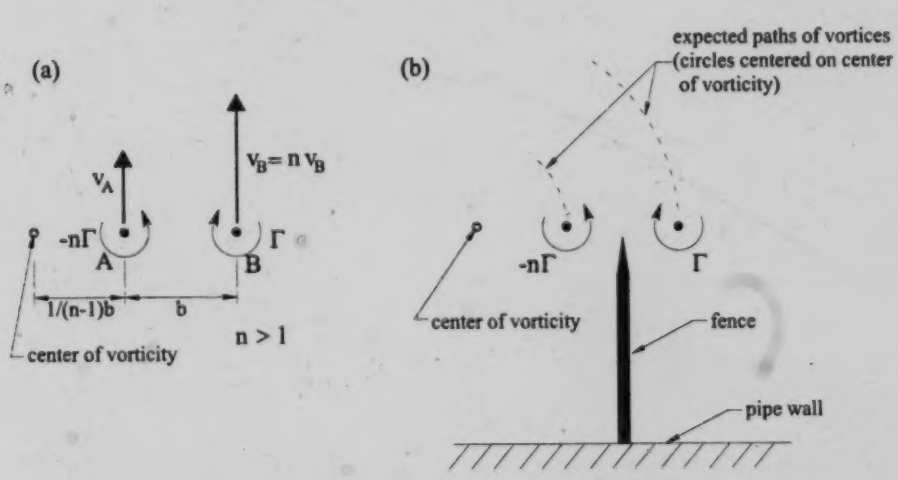

Figure 2.22: Basic mechanism for synthetic fence jet vectoring: two point vortices of unequal circulation magnitude, one of opposite sign and magnified strength by the factor n. (a) Shows the induced velocities of two vortices of unequal circulation and the location of the Center of Vorticity. Γ is the circulation, v_A is the induced velocity of vortex A by vortex B, v_B is the induced velocity of vortex B by vortex A. (b) Shows the path that these vortices would follow according to 2-D point vortex theory.

Another way of explaining this circular path that comes out of the idealized case is by recognizing that the center of vorticity must remain constant. Leonard (1980) states that for "two-dimensional flows at rest at infinity and with no interior boundaries ..." the total circulation and the linear impulse must be invariants. These conditions are given mathematically for N two-dimensional point vortices by Equations 2.1 and 2.2.

$$\sum_{i=1}^{N} \Gamma_i = const \tag{2.1}$$

$$\sum_{i=1}^{N} \Gamma_i \overline{x}_i(t) = const \tag{2.2}$$

$$\frac{\sum_{i=1}^{N} \Gamma_i \overline{x}_i(t)}{\sum_{i=1}^{N} \Gamma_i} = \overline{X} = (X, Y) = const \tag{2.3}$$

The center of vorticity can be defined by equation 2.3 and must also be constant (Batchelor, 1967). For a pair of two-dimensional point vortices of unequal opposite sign circulation, the center of vorticity is shown in Figure 2.22. Batchelor (1967) states that "in the case of just two vortices, the distance [b] between them must remain constant and the two vortices move in circular paths about the center of vorticity ...". For more than two vortices "...the details of motion are not evident, but the above invariants suggest that all [of the] vortices remain within a distance of order D from the centre of vorticity..." (Batchelor, 1967) where D is defined as:

$$D = \sqrt{\frac{\sum_{i=1}^{N} \Gamma_i \{(x_i - X)^2 + (y_i - Y)^2\}}{\sum_{i=1}^{N} \Gamma_i}}. \tag{2.4}$$

This suggests that even if there are more than two vortices, as long as there remains an inequality in the vorticity, the average motion of the vortices should follow a circular path around the center of vorticity.

This is for an infinite fluid. In the case of the synthetic fence jet there are walls therefore the image vortices should be considered. We are neglecting this effect in this first order explanation of the phenomenon. Also, we considered only 2 two-dimensional ideal point vortices. These idealizations could be the reason that a circular path results rather than the straight vectored jet which occurs in the experiments.

2.3.2.2 Vorticity Generation

Here we will discuss the generation of vorticity in order to show where the inequality in vorticity originates. First we will review Γ generation for a general velocity at separation u_s, and then we will propose a waveform that captures the characteristics necessary for a vectored synthetic fence jet.

We will find the rate that circulation passes through a surface extending out of the boundary layer from the edge of the fence. Consider the case of an infinite flat plate with an infinitely long fence in a semi-infinite oscillating flow field as seen in Figure 1.1 in Section 1.2. As the flow approaches separation at the edge of the fence from either direction, the total circulation in any

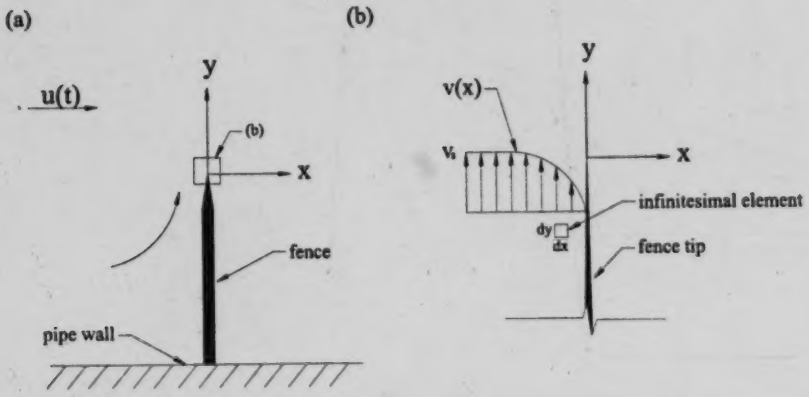

Figure 2.23: Generation of vorticity at the fence's edge. (a) Shows the general geometry. (b) Shows a close-up view of the details at the fence's tip. The vorticity in the vortices shed from the edge of the fence comes from the boundary layer.

infinitesimal element of area $dxdy$ at the fence's edge will be the area times the vorticity in the element. This is depicted in Figure 2.23.

The rate of change, then, is simply:

$$\frac{d\Gamma}{dt} = \omega \frac{dxdy}{dt}. \tag{2.5}$$

Also, we know that the velocity in the direction along a streamline is the time derivative of the position y.

$$v = \frac{dy}{dt} \tag{2.6}$$

Although the flow is near the fence edge, we assume that the flow is like

a flat plate boundary layer which does not vary along the length of the plate. Since we are assuming 1D flow, the velocity and the vorticity will be functions of x and not y. Therefore,

$$\frac{d\Gamma}{dt} = \omega(x)v(x)dx. \tag{2.7}$$

We can replace $\omega(x)$ with $\frac{dv}{dx}$ because ω is defined as $(\frac{dv}{dx} - \frac{du}{dy})$ and $\frac{du}{dy} = 0$ since it is approximately parallel laminar boundary layer flow.

Integrating with respect to x from zero to negative infinity [2]

$$\frac{d\Gamma}{dt} = -\int_0^{-\infty} \frac{dv}{dx}v(x)dx = -\int_{v(0)}^{v(-\infty)} v(x)dv. \tag{2.8}$$

This results in

$$\frac{d\Gamma}{dt} = -\frac{v^2}{2}\Big|_{v(0)}^{v(-\infty)}. \tag{2.9}$$

At $x = 0$, $v = 0$ and as $x \to -\infty$, $v \to v_s$ which is the velocity at the edge of the boundary layer at separation, therefore

$$\frac{d\Gamma}{dt} = -\frac{v_s^2}{2}. \tag{2.10}$$

A more general variation of this result for the separation of a boundary layer is given by Leonard (1980). The rate that circulation leaves the fence

[2]We integrate from the fence where $x = 0$ out of the boundary layer where $x \to -\infty$. The negative infinity and the negative before the integral are due to the coordinate system and flow direction chosen (see Figure 2.23).

is proportional to the velocity squared. The total circulation introduced to the flow from the fence per cycle when velocity is in one direction is given by,

$$\Gamma = -\int \frac{v_s^2}{2} dt. \tag{2.11}$$

We would like to know what the required properties are for a waveform to produce a vectored jet. We propose the simplified waveform seen in Figure 2.24. It has the critical characteristics that are similar to the waveform produced by the damaged power oscillator, Figure 2.19. They are the high amplitude peak velocity u_R and short duration τ_R in a direction to the right and the lower amplitude peak velocity u_L with longer duration τ_L to the left. Once the peak magnitudes and one duration are prescribed, the remaining duration is determined by the zero mass flux requirement of a periodic acoustic wave.

Let us now examine the vorticity generated for this waveform. From Equation 2.11 we know that the circulation of the vorticity generated is proportional to the integral of the separation velocity squared. For sections of the waveform where velocity is constant we can remove the velocity from the integral resulting in a simplified equation.

$$\Gamma = -\frac{v_s^2}{2} \int dt \tag{2.12}$$

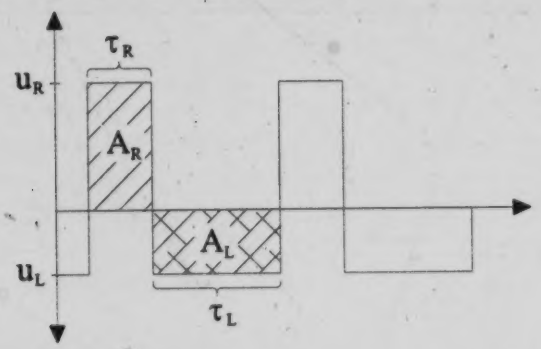

Figure 2.24: Proposed simplified waveform to produce vectored jetting. The velocity to the right is of higher amplitude and shorter duration than the velocity to the left. This is the characteristic of the damaged power oscillator waveform (Figure 2.19) that we believe to be responsible for vectored jetting.

$$\Gamma = -\frac{v_s^2}{2}\tau \qquad \text{where } v_s \text{ is constant} \tag{2.13}$$

The separation velocity, v_s is proportional to the freestream velocity u, therefore

$$v_{Rs} = ku_R \tag{2.14}$$

$$v_{Ls} = ku_L, \tag{2.15}$$

Where k will be taken as a constant for our purposes here. This means that for the waveform of Figure 2.24 the circulation produced at a fence for the flow in the positive direction and the negative direction will respectively

be

$$\Gamma_R = -k\frac{u_R^2}{2}\tau_R \qquad \text{and} \tag{2.16}$$

$$\Gamma_L = +k\frac{u_L^2}{2}\tau_L. \tag{2.17}$$

By continuity, in order to have zero net mass flux in the x direction as an acoustic wave would, the total area under the $v - t$ curve must be zero. Therefore in Figure 2.24 the area A_R must be equal to area A_L. If u_R is equal to $n \cdot u_L$, τ_R must be equal to τ_L divided by n. Substituting this into Equation 2.16 gives

$$\Gamma_R = -k\frac{(n \times u_L)^2}{2}\frac{\tau_L}{n} = -n \underbrace{\left(k\frac{(u_L)^2}{2}\tau_L\right)}_{\Gamma_L, \text{ see Eq. 2.17}} \tag{2.18}$$

therefore

$$\Gamma_R = -n\Gamma_L. \tag{2.19}$$

The circulation generated in a particular cycle varies as the square of the velocity and linearly with time. As a result, more circulation can be generated during flow in one direction than in the other.

This unequal generation of positive and negative circulation is an important link to explain why the jet from this waveform is vectored. As discussed

in Section 2.3.2.1 if there are two unequal vortices of opposite sign then the vortices will follow a circular path turning towards the stronger vortex as seen in Figure 2.22. It follows that a sequence of pairs would behave qualitatively similarly.

2.3.2.3 Synthesized Vectored Jet Waveform

Now that we have a theory explaining why the vectored jet occurs, we can try to control the vectoring of the jet. Rather than rely on the damaged power oscillator, we created a waveform that should produce a vectored jet that can be mathematically defined and easily modified. The waveforms used are shown in Figure 2.25. The equation that defines this set of waveforms is:

$$V = \left(\frac{1}{5 + 4\sin(2\pi f t)}\right)^{\eta} + C. \tag{2.26}$$

The C is simply a constant to reduce the DC offset. The variable η is used to define the character of the function. As η is increased, the difference in the velocities and in the durations in each direction is also increased.

A Matlab® function was used to create a computer sound file that had this waveform. The output from the computer sound card was then routed to the amplifier to produce the signal at the speaker. A vectored jet was produced and the direction that it was vectored could be reversed by swapping the leads to the speaker. Also, it was observed that the amount of vectoring could be altered by changing η. For large values of η, the angle of the vectoring of

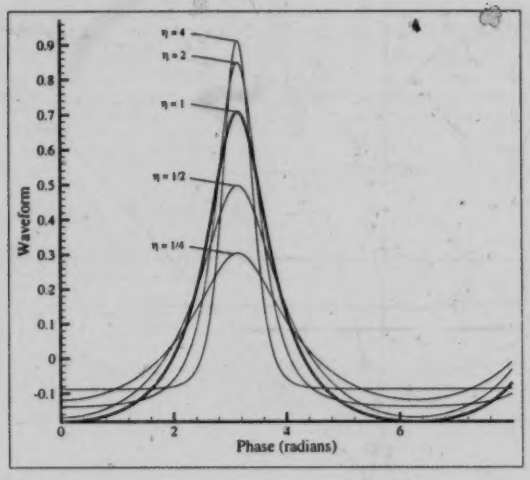

Figure 2.25: Synthesized waveform to produce vectored jetting

the jet from normal became larger. For smaller values of η, the angle of the vectoring was reduced.

2.4 Conclusions

Smoke-wire flow visualization and image correlation velocimetry (ICV) were used to confirm the existence of and then study the jet created when a fence is introduced to an acoustic wave in a pipe. This jet has been named a synthetic fence jet (SFJ).

These jets only exist under certain forcing conditions. In the experimental setup used the acoustic response of the pipe limits the frequencies at which jets can be created. The lowest Strouhal number at which a jet was found

was 0.43 and the highest Strouhal number was 10.16. These were also the limits of Strouhal number that could be achieved in the experiments. At the upper limit of Strouhal number the amplitude of the forcing was low enough to allow the buoyancy of the smoke to dominate the flow. At the lower limit the amplifier and speaker began to distort the signal. The lowest Reynolds number that a jet was produced was 65 and the highest was 1950.

For the circular pipe and fence used in the experiments, the jetting occurred only near the middle of the fence and not along its entire length. This occurred for the entire range of successful forcing parameters used.

We took the average velocity of the jet at the center of the pipe to represent the jet velocity. The ICV results show that there are larger measured fluctuations in the 5 photograph averaged velocity field at the centerline for a Strouhal number of 1.6 and for a Reynolds number of 620. These fluctuations are due to the high turbulence intensity expected in this highly forced unsteady flow combined with an insufficient number of photographs to determine an actual steady average. For higher Strouhal numbers the scatter in the calculated velocity fluctuation is significantly reduced. The maximum velocity ratio (U_j/U'_{fence}) for a Reynolds number of 620 was found to be approximately 0.94 at a Strouhal number of 1.6. The minimum velocity ratio was found to be approximately 0.14 at a Strouhal number of 0.68. The maximum velocity ratio averaged for all the data at each Strouhal number for a Reynolds number of 620 was found to be 0.55 at a Strouhal number of 1.8.

While the vortex structure of the SFJ for lower Reynolds numbers appears

to be a chain of vortex rings, there is evidence that suggests that they do not come immediately from the forcing. The frequency of the large scale structure was estimated to be about $1/20^{th}$ of the forcing frequency. This suggests that there is a somewhat more complex creation mechanism than simply periodic separation from the fence at the forcing frequency. This could be explained by approximately 4 pairings of the created vortices, or by an initially laminar jet developing the lower frequency instability.

The jet could be vectored along the pipe axis by altering the forcing waveform. A theory was developed that explains this phenomenon. The amount of vorticity produced during the portion of the flow in either direction is linearly proportional with time but is proportional to the square of the velocity. As a result of this, there is more vorticity formed when the flow is fast but for a shorter time than is formed when the velocity is slow but for a longer time. This relation between time and velocity is required for zero net mass flux along the pipe axis as would be associated with an acoustic wave. Neglecting the presence of boundaries, the center of vorticity is an invariant (Batchelor, 1967). This means that the vortices will tend to follow a circular path about the center of vorticity. The jet will tend to turn in one direction or the other. This vectoring is also explained using the Biot-Savart law of fluid mechanics. By idealizing the vorticity created during each half cycle as a discrete point vortex and neglecting the boundaries, we can use the Biot-Savart law to easily predict the path that the vortices will follow. The velocity of the weaker vortex, induced by the stronger vortex, will be

greater than the velocity of the stronger vortex, induced by the weaker vortex. Therefore the weaker vortex will move ahead of the stronger vortex resulting in the vortex pair turning towards the stronger vortex.

There are still unanswered questions about the actual vortex structure and the response of the SFJ to forcing parameters.

BIBLIOGRAPHY

Batchelor, G. (1967). *An introduction to fluid dynamics.* Cambridge University Press.

Chapple, D. (1998). The role of turbulence in pulsation induced orifice plate flow metering error. Master's thesis, University of Alberta.

Chen, T. (2001). Personal communications.

Corke, T., Koga, D., Drubka, R., and Nagib, H. (1977). A new technique for introducing controlled sheets of smoke streaklines in wind tunnels. *ICIASF 1977 Record, IEEE Publication*, pages 74–80.

Leonard, A. (1980). Vortex methods for flow simulation. *Journal of Computational Physics*, 37(3):239–335.

Papamoschou, D. and Bunyajitradulya, A. (1997). Evolution of large eddies in compressible shear layers. *Physics of Fluids*, 9:756–765.

Sigurdson, L. (1986). *The structure and control of a turbulent reattaching flow.* PhD thesis, Calif. Inst. Technology.

Chapter 3

Image Correlation Velocimetry

3.1 Introduction

In this section we will discuss image correlation velocimetry (ICV), (Tokumaru and Dimotakis, 1995). We will begin by explaining why we decided to use ICV and then explain what ICV is. Then we'll explain how we validated and used it.

Due to the complex flow structures of the synthetic fence jet (SFJ) it is very difficult to obtain velocity data. The flow is completely three dimensional and fully reversing along the pipe axis direction. Hot-wire anemometers are unable to distinguish flow direction and are therefore unsuitable for measuring the velocities.

3.2 Theory

This section contains the theory behind the ICV technique, a review of techniques, and a more detailed look at ICV specifically. We will then discuss

the details of the ICV technique used by Papamoschou and Bunyajitradulya (1997) which was used as the basis for our technique.

3.2.1 Background and Literature Review

The idea of using multiple images to obtain velocity information is not new. Recently researchers have been using film and digital cameras to obtain images that are then processed by computers to obtain velocity field information. These methods include ICV, particle image velocimetry (PIV), digital particle image velocimetry (DPIV), and even stereoscopic PIV.

The basis for these techniques is the same. The flow is seeded with some form of flow visualization. Two consecutive images of the flow at slightly different times are obtained. Portions of the images are matched to determine the displacement of the flow from which the velocity can be calculated. What varies is the flow visualization technique, the method that the images are obtained and the way in which portions of the images are matched. The main difference between PIV and ICV is in the images that are used to obtain the velocity field. For PIV the images consist of distinct particles. For ICV the image is a scalar field which may or may not include images of discrete particles. The focus of this thesis is on ICV used on a scalar field without imaging discrete particles. A good review of PIV techniques is given by Adrian (1991).

The nomenclature used for these various image-based velocimetry techniques is quite varied. The term image correlation velocimetry (ICV) was

proposed by (Tokumaru and Dimotakis, 1995). They use this term to describe their particular method and explain that the reason they use this terminology is that the method is not limited to a specific type of image. We have elected to use this same nomenclature to describe the method that we used which is based on the work of Papamoschou and Bunyajitradulya (1997) because the terminology is an accurate description of the method. Papamoschou and Bunyajitradulya (1997) use the terminology "cross-correlation method" to describe the computational method that they implement. Also, in keeping with the spirit of the original justification for creating the name ICV, the method should work well on a broad range of image data including particle images and scalar images.

We will discuss two computational techniques for ICV. The first is a gradient technique used by Tokumaru and Dimotakis (1995). In this method the gradients in the scalar image are correlated to obtain the velocity. The second method, which is referred to as the 'cross-correlation method', implemented by Papamoschou and Bunyajitradulya (1997), is much simpler computationally and relies on the brightness of the pixels to obtain the velocity information. The gradient method used by Tokumaru and Dimotakis (1995) allows for rotation and deformation of the regions being analyzed while the cross-correlation method allows only for translation of the regions being analyzed. The cross-correlation method could also be expanded to allow rotation of the regions being analyzed but at a large computational cost. We decided that the additional complications of the gradient method

outweighed the benefits for our purposes therefore we decided to use the cross-correlation method.

Papamoschou and Bunyajitradulya (1997) have investigated the motion of large eddies in supersonic shear layers using the cross-correlation method. They used planar laser-induced fluorescence of acetone to visualized the flow. A CCD camera was used to capture the images. Rather than take two separate images, they used an offset double exposure. The resulting image contained the initial position of the eddy in the left half of the image and the later position of the eddy in the right half of the image. A 'template' or correlation window that contained the eddy was then chosen in the left half of the image. This correlation window was then moved throughout the entire image performing a cross-correlation between this correlation window and the image at each location. The correlation they used was

$$C_{TF}(\xi,\eta) = \frac{1}{MN}\sum_{\xi=0}^{M}\sum_{\eta=0}^{N} T'(x,y)F'(x+\xi,y+\eta) \tag{3.1}$$

where M and N are the width and height of the correlation window, $C_{TF}(\xi,\eta)$ is the correlation at the location ξ units from the left side of the image and η units from the bottom of the image, $T'(x,y)$ is the difference of the acetone concentration from the spatial average over the correlation window and $F'(x+\xi,y+\eta)$ is the difference of the acetone concentration from the spatial average over the same area at locations ξ and η of the original image. The correlation coefficient, which has a value of one for

perfect correlation, is given by

$$R_{TF}(\xi,\eta) = \frac{C_{TF}(\xi,\eta)}{\sqrt{C_{FF}(\xi,\eta)C_{TT}}} \tag{3.2}$$

where $R_{TF}(\xi,\eta)$ is the correlation coefficient, $C_{TF}(\xi,\eta)$ is the correlation as defined above, $C_{FF}(\xi,\eta)$ is the autocorrelation for the area at locations ξ and η, and C_{TT} is the autocorrelation for the correlation window. Papamoschou and Bunyajitradulya (1997) found a perfect correlation at the original location and a very high correlation in the right half of the image where the eddy had moved to. The displacement of the correlation window from its original location to the best correlation in the right half of the image then gives the displacement of the eddy during the time interval between exposures. The velocity is of course, the displacement in each direction divided by the time interval Δt between exposures.

Papamoschou and Bunyajitradulya (1997) used correlation window sizes of 150 pixels by 150 pixels and searched the entire image for the solution. The image sizes were as large as 384 pixels by 576 pixels. The computational time was very high at "...an average of five hours to process on a Pentium 100 computer."

Murakami and Papamoschou (2000) also used the same computational and experimental method to study coaxial supersonic jets.

3.3 Preliminary Experiments

In order to determine the viability of the ICV method for the synthetic fence jet a number of experiments were performed. In this section we will describe these preliminary experiments and give the results.

3.3.1 Double Exposure

To begin with we wanted to see if it was possible to obtain velocity information from the smoke-wire flow visualization photographs by using a multiple exposure photograph. To perform this experiment, the camera shutter was opened and the strobe was fired twice. The smoke from the flashes of the strobe were almost completely indistinguishable from each other. There were some features that appeared as though they might have been from the separate flashes of the strobe but the confidence in any velocity results was low. We decided that we required a method that would allow us to obtain separate images.

3.3.2 Time Series - 'Burst Mode' on Camera

In order to obtain a series of photographs the camera was set on 'burst' mode. In 'burst' mode the camera will take a series of photographs in a row. This would allow us to obtain separate photographs of the different times.

In order to accurately determine the elapsed time between photographs, an analogue timer with a resolution of 10 ms was positioned in the field of

view. The camera was set on 'burst' mode and the timing of the various components were set up so that the camera would fire while the leading edge of the smoke was just leaving the smoke wire. The camera could only fire at a rate of approximately 4 frames per second. To minimize the time between photographs, the mirror on the camera was locked up.

To obtain an approximate velocity, the distance between the fence's edge and the smoke front was measured on the photographs. The actual distance was determined knowing the pipe diameter. Also, the time elapsed between photographs was found from the analogue timer visible in the photographs. Using this information, the average velocity of the smoke front over the time interval between photographs was determined.

Two pairs of consecutive photographs are shown in Figures 3.1 and 3.2 and Figures 3.3 and 3.4. Both of these sets of photos were for a U' of 0.32 m/s and a frequency of excitation of 42 Hz. The Strouhal number for these forcing parameters is 3.2. The resulting Δt for the first set was 0.26 s and the measured displacement was about 30 mm. The calculated jet velocity is found to be 117 mm/s. The results for the second set were found to be identical. This suggests approximate repeatability.

This technique will work only for very low velocities due to the space constraints. For larger velocities the displacement would be too large and the flow of the smoke front will interact with the opposite wall of the pipe. In order to avoid this problem we would have to decrease the Δt which could not be done with the camera that was used. Also, the only feature that can

be correlated in the image is the smoke front because the features in the smoke have had enough time to change too much. This means that only a crude estimate of the velocity can be obtained. If the Δt were reduced then there would be less distortion of the smoke and a more sophisticated ICV method might work. In order to reduce the Δt we would have to either use two cameras or else use a double exposure method.

3.3.3 One Flash, Two Flash, Red Flash, Blue Flash

We wanted to know if we could use 2 stroboscopes and put colour filters over them and expose a single frame with consecutive images at slightly different times in different colours. The perceived advantage of this method over using two cameras is that the alignment of the two cameras would be very critical. The images from each camera would have to be scanned separately and the stationary features in the images would have to be carefully aligned. In the case of the strobes, we believed that the strobes could be positioned so that they light the same field of view and that the alignment would be less critical than for the multiple camera method. Also, there would be only one image containing all of the desired information. One camera with a double image capture capability would also work well, but was not currently available.

One of the difficulties encountered when using two stroboscopes with colour filters was in achieving proper illumination. The quality of the result was highly dependent on the filters used and the positioning of the strobes.

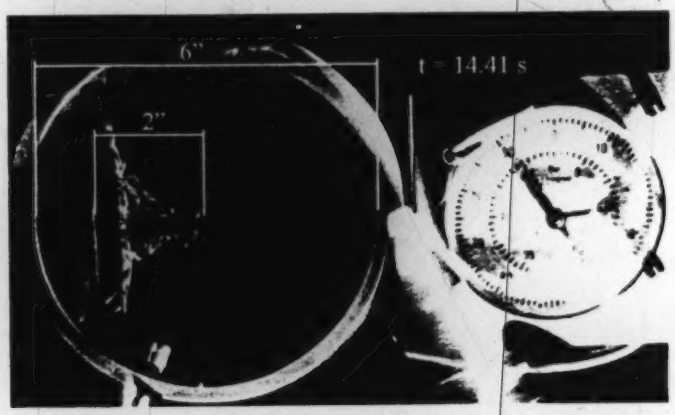

Figure 3.1: 'Burst' photograph: first in series. Position of smoke front as measured from the fence's edge determined using the pipe diameter as a reference length. The time of the photograph is determined by the analogue timer visible in the photograph. Parameters: h=25.4 mm (1"), f_{ex} = 42 Hz, U'_{fence}= 0.32 m/s, St=3.2, Re=521.

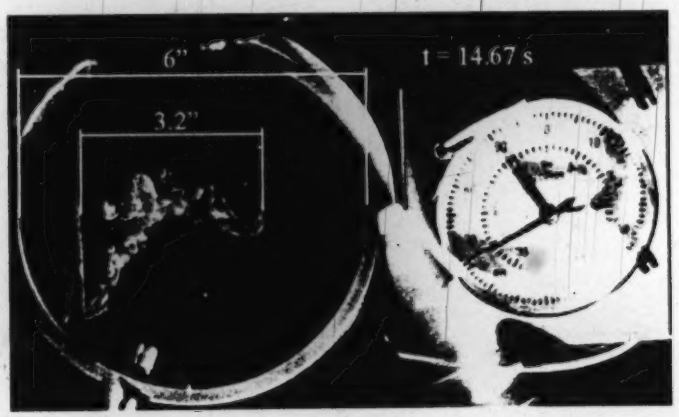

Figure 3.2: 'Burst' photograph: second in series. Position of smoke front as measured from the fence's edge determined using the pipe diameter as a reference length. The time of the photograph is determined by the analogue timer visible in the photograph. Parameters: h=25.4 mm (1"), f_{ex} = 42 Hz, U'_{fence}= 0.32 m/s, St=3.2, Re=521.

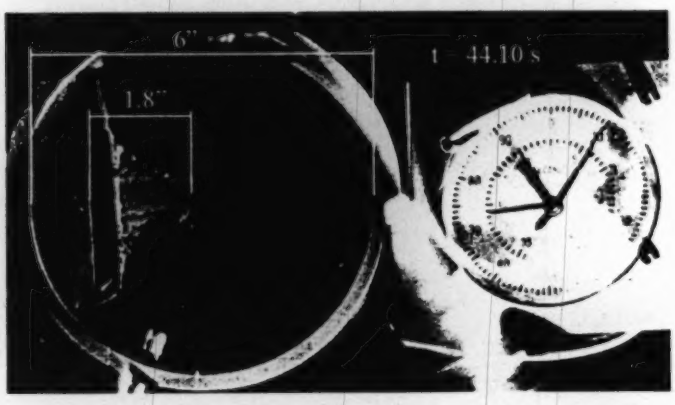

Figure 3.3: 'Burst' photograph: first in series. Position of smoke front as measured from the fence's edge determined using the pipe diameter as a reference length. The time of the photograph is determined by the analogue timer visible in the photograph. Parameters: h=25.4 mm (1"), f_{ex} = 42 Hz, U'_{fence}= 0.32 m/s, St=3.2, Re=521.

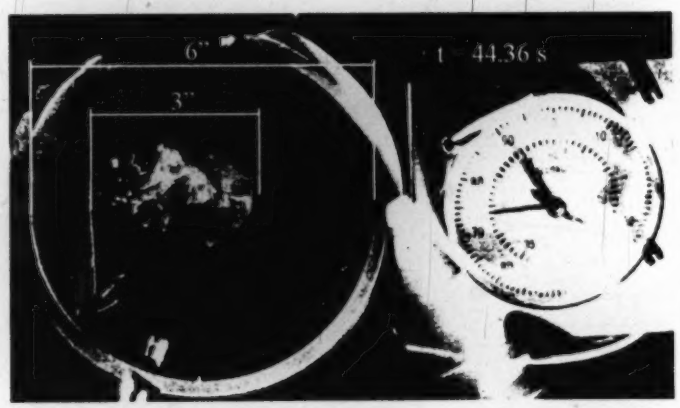

Figure 3.4: 'Burst' photograph: second in series. Position of smoke front as measured from the fence's edge determined using the pipe diameter as a reference length. The time of the photograph is determined by the analogue timer visible in the photograph. Parameters: h=25.4 mm (1"), f_{ex} = 42 Hz, U'_{fence}= 0.32 m/s, St=3.2, Re=521.

3.3.3.1 Filters

The choice of filters used for the colour separation is very important. For the preliminary testing a set of Lee® filters were used. These filters were not designed for color separation work and therefore allowed a wider visible spectrum of light through. When the red and blue components of the image were separated a shadow of the other component remained. A set of Kodak® color separation filters were then used which provided much purer color separation. When the blue and red components of the photograph were extracted the resulting images showed very little of the other component.

3.3.3.2 Strobe Positioning

Initially the Stroboscopes were positioned as closely as possible to the pipe to provide the maximum illumination. In order to achieve this they had to be mounted at an angle of approximately 75 degrees from each other as seen in Figure 3.5. Light columnators were placed over each stroboscope. These consisted of two 25.4 mm (1") by 140 mm (5.5") slits separated by approximately 127 mm (5"). One of the slits was directly over the strobe and the other was supported 127 mm (5") away above the strobe. As a test of the technique photos were taken where the strobes were fired simultaneously. Ideally, the extracted red and blue components of these photographs should be identical. Upon inspection there were large differences between these components. The stroboscopes were moved further from the pipe and the angle between them reduced to approximately 20 degrees in an attempt to

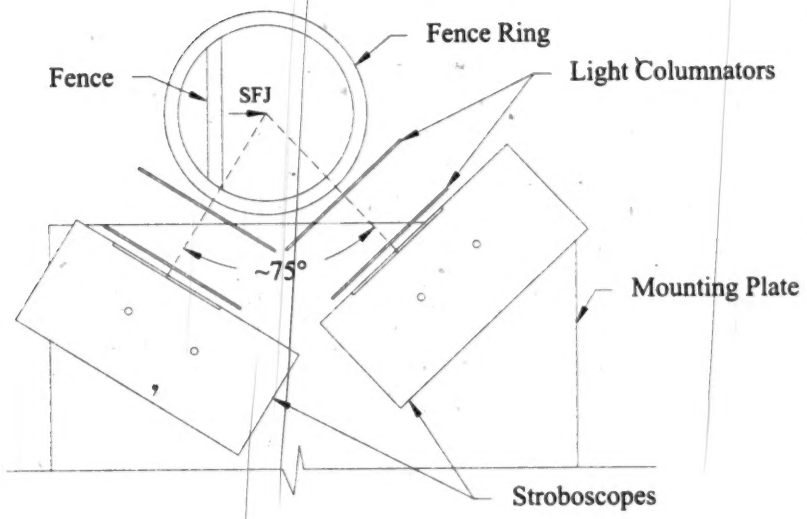

Figure 3.5: Initial stroboscope mounting schematic. Strobes mounted at approximately 75° apart. One strobe was covered with a red filter and the other was covered with a blue filter. Light columnators each consisting of two 25.4 mm (1") wide by approximately 140 mm (5.5") long slits separated by approximately 127 mm (5″) were placed over each stroboscope to produce a 25.4 mm (1″) sheet of light.

improve the results. They were significantly improved but still not perfect. The problem was that the light sources were coming from different physical positions and therefore the illumination field was different, making it more difficult to correlate the two images in a useful way. In order to get the two light sources to appear to be one, a beam splitter was used.

3.3.3.3 Beam Splitter Apparatus

The idea was to use a beam splitter to combine the two light sources and make them appear as one. A beam splitter is a mirror that allows half of the light to be transmitted and half of the light to be reflected. The apparatus was designed to hold the two stroboscopes and the beam splitter in perfect alignment so that the light sources would appear identical. A schematic of the beam splitter apparatus is shown in Figure 3.6. One of the problems with this setup is that half of the light from each stroboscope is directed away from the area of interest. The main advantage is that differences between illumination fields of the red and blue components of the resulting image were reduced significantly. Figures 3.7 and 3.8 show the difference between the red and blue components of the image data for simultaneous strobe photographs when the stroboscopes are mounted at 20° from each other and when the beam splitter apparatus is used respectively. The maximum difference between the red and blue components in the jet region of the photograph with the beam splitter apparatus was 53 as compared with 61 when the beam splitter was not used. This shows a 14% reduction in the difference. These values are the pixel

intensity in the image file and are representative of the light intensity. The Kodak colour separation filters were used for both of these cases. The red and blue components were extracted directly from the TIFF[1] image data. It is clear that the differences between the red and blue components are reduced when the beam splitter apparatus is used.

3.3.3.4 Scanning

Digitizing the photographs was very important to using an ICV method. Preliminary work was done using a flatbed Hewlett-Packard® Scanjet II scanner that was readily available in the department. This scanner has an optical resolution of 600 dots per inch (dpi) and the software allowed interpolation to very high resolutions. We scanned the slides at an interpolated resolution of 1200 dpi for the majority of the testing using this scanner[2]. The results using this scanner appeared quite good. One of the problems with this low resolution is that the error in calculated velocity due to uncertainty in pixel displacement must be ± 1 pixel. For example, when the pixel displacement of the correlated images due to physical displacement of the scalar being visualized is 5 pixels this "pixel error" becomes $\pm 20\%$. We believe that the ICV would work best if the physical displacement was minimized because there would be less distortion of the smoke between images. In order to increase the pixel displacement for a given physical displacement a higher resolution

[1] The images were scanned as RGB (red, green, and blue) Tagged Image File Format (TIFF) image files.

[2] We were unaware that the scanner had an optical resolution of only 600 dpi and that the 1200 dpi setting was interpolated.

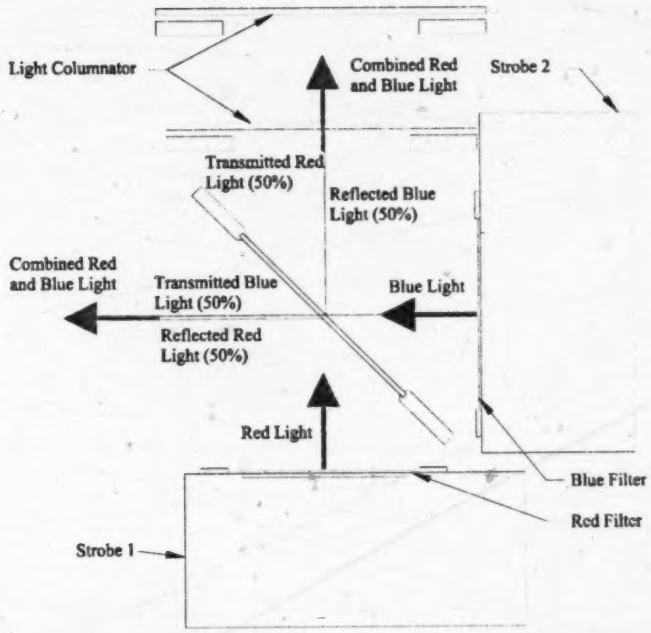

Figure 3.6: Beam splitter apparatus light schematic. Purple indicates the combined red and blue light. Half of the light from each stroboscope is reflected and half is transmitted by the beam splitter. This results in the light from the red and blue stroboscopes appearing to come from the same location.

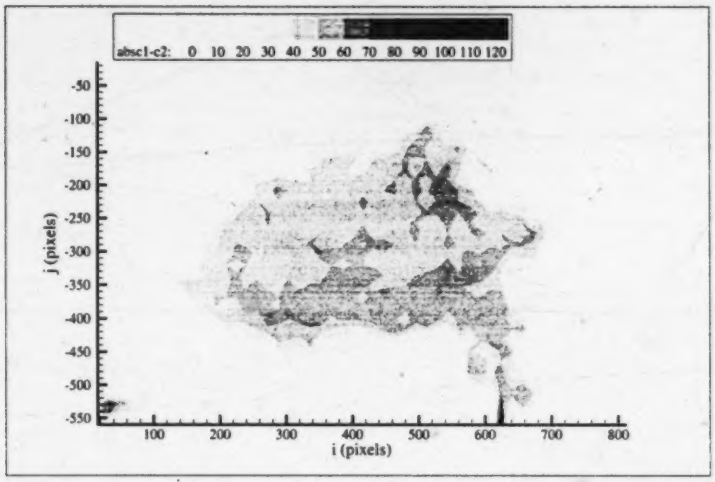

Figure 3.7: Difference between red and blue components for simultaneous strobe photograph of the SFJ with strobes mounted 20° apart. The units are in pixel intensity for the 24 bit true colour TIFF image file.

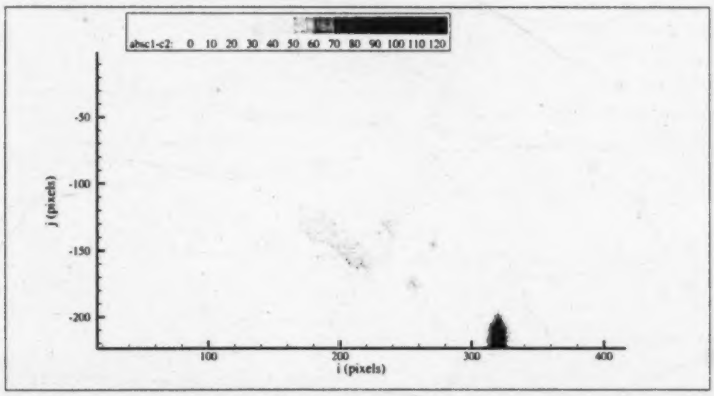

Figure 3.8: Difference between red and blue components for simultaneous strobe photograph of the SFJ with beam splitter apparatus. The units are in pixel intensity for the 24 bit true colour TIFF image file.

scanner was purchased. The Minolta® D'Image Scan Dual II was chosen. This is a slide/negative scanner with an optical resolution of 2820 dpi.

When using this scanner a new problem was encountered. The ICV would report zero velocities, particularly in the middle of a large cloud of smoke. The ICV continued to appear to work correctly around the edges of the smoke where there were more gradients in the smoke.

Upon inspection of the results and the digitized images a probable cause of the problem was discovered. The resolution of the scanner is sufficiently high to capture the grain of the film. For some of the SFJ photographs the ICV would lock onto the grain rather than the image data.

In order to reduce this problem we used an image filter from Adobe® Photoshop® called 'Dust & Scratches'. This filter was reported to help eliminate the grain by an instructional book for Adobe Photoshop. After applying the filter, the images did appear smoothed but the ICV began to work significantly better. To justify the use of this filter we compared the results of a normal jet validation experiment with and without this filter applied. The results are given in Section 3.5.3. This filter was used on all of the SFJ data to be consistent. The filter was not required or used for the pipe flow experiment that is described in Section 3.5.4.

3.4 Dr. Tony Chen's ICV Code

3.4.1 Introduction

We decided to use the cross-correlation technique discussed in Section 3.2 due to its simplicity. Dr. Tony Chen, a post-doctoral student, wrote a computer code based on the method used by Papamoschou and Bunyajitradulya (1997). The code was written in C. In order to allow flexibility in the parameters an initialization file was used to input a number of parameters. The parameters are detailed in Appendix A.

3.4.2 How the Code Works

Here we will describe how the ICV code works and explain some of the differences between the method used by Papamoschou and Bunyajitradulya (1997) and our method.

The correlation equations we used are the same as were used by Papamoschou and Bunyajitradulya (1997). This is described in Section 3.2.1.

The most important difference between our method and the method used by Papamoschou and Bunyajitradulya (1997) is that we do not apply the cross-correlation across the entire image. We recognize that there is some maximum displacement for any particular portion of the image in the time between images. We limit the cross correlation to a region that is a reasonable distance from the original location. This means that the code will run significantly faster because it doesn't have to perform as many calculations.

If a solution is not found within that region then a variable is output indicating that this is the case and the code can be run again with an increased searching distance.

Another important difference in the way that we use this method is that we calculate a velocity field rather than a single velocity of a large scale structure. The correlation window must be large enough to contain some flow structure so we do not expect to obtain the internal velocity field to the fine scale flow features that might exist.

Finally, in order to improve the result, we implemented an error correction method called "Correlation Based Correction" (CBC). This method was used by Hart (2000) for PIV error correction. When performing the cross-correlation on the images a correlation table is produced. This correlation table is essentially a set of correlation coefficient values for each location that the correlation window has been moved to and a cross-correlation performed. The CBC method involves the element-by-element multiplication of two or more adjacent correlation tables. For example, if we are trying to find the velocity at the point (i, j) in the image then we could find two correlation tables: one δi to the right $(i+\delta i, j)$ and one δi to the left $(i-\delta i, j)$. We would then multiply these tables element by element and obtain a new correlation table. The location of the maximum peak in this resulting correlation table would be taken as the solution at the point (i, j). These correlation tables must overlap each other. In other words the correlation window half-size must be greater than the shifting of the correlation tables, δi. The effect of

this method is to eliminate "any correlation value that does not appear in each of the combined correlation tables ..." from the resulting table (Hart, 2000). Peaks due to noise are unlikely to appear at the same location in both correlation tables. When the correlation tables are multiplied, any peak in one correlation table that is not in the other will be removed leaving only the peaks that appear in both correlation tables. The remaining maximum peak is likely to be the correct solution. Hart (2000) also discusses improvements in subpixel accuracy for PIV measurements with CBC. These do not apply in the case of ICV because subpixel interpolation is not implemented. One of the problems that we encountered while using the CBC error correction method is that the running time of the code was increased significantly. This is because more calculations are being performed. When two correlation tables are used there are approximately twice as many calculations performed. When four tables are used, there are four times as many calculations.

3.4.2.1 Acceleration of the Code

During the testing of the ICV method we found that for the high resolution images it could take a very long time to obtain a complete solution. For some of the images it took as long as 25 hours to run the code[3]. Sometimes the parameters chosen needed to be modified and the code run again in order to obtain a better solution. For this reason it was important to improve the speed of the code.

[3]Calculating a full vector field on a high resolution 30 MB image with two correlation table CBC error correction on a Pentium 800 MHz computer

A multi-grid scheme could be implemented to accelerate the code. By reducing the resolution of the image we can increase the speed of the code. The solution at the lower resolution can then be passed as an initial guess to a higher resolution run and the search area in the higher resolution image can be reduced significantly. This was implemented with two levels of resolution reduction. The image resolution is reduced to half and quarter of the original resolution. The correlation is performed first on the quarter resolution image and the solution is used as an initial guess for a correlation on the half resolution image. Similarly, the solution from the half resolution correlation is used as an initial guess for a correlation on the full resolution image. In some cases the running time was reduced from 25 hours to just 10 minutes. The solution from the original unaccelerated version was compared with the solution from the accelerated version for a number of test cases. The final solution remained the same for all of them. This type of acceleration technique has been used before by Reza et al. (1999) and others.

3.4.2.2 Output From the Code

The output from the code is in a simple ASCII data file in point format that is compatible with Tecplot® . Point format means that there is a column for each variable that is output and the dimensions of the data are given at the beginning of the file. The variable names along with some other formatting information are also listed at the beginning of the file. The date and time as well as the running time of the code are listed at the very beginning of the

file as well. The variables that are output and descriptions of them are:

i is the horizontal pixel location measured from the left side of the image.

j is the vertical pixel location measured from the top of the image.

c1 is the intensity of the red component at the location (i,j) in the original image.

c2 is the intensity of the blue component at the location (i,j) in the original image.

correlation is the value of the maximum correlation coefficient for the velocity calculation at point (i,j).

u is the calculated horizontal displacement in pixels. This is converted to velocity by using a conversion between pixels and meters and dividing by the elapsed time between strobe flashes.

v is the calculated vertical displacement in pixels. This is converted to velocity as described in u above.

The data files were opened using Tecplot® 7.0 and plotted using features that were built into Tecplot. Using Tecplot the average pixel intensity of the red and blue components was calculated to give a representative smoke density. Tecplot also has a number of built in equation functions that allowed us to convert the data to physical velocities. The conversion between pixels and meters was determined using a grid photograph. The grid was

placed in the test section and a photograph was taken of it. An example of the grid photograph used for the SFJ photographs is given in Figure 3.9 and an example of the grid photograph from the turbulent pipe flow experiment (Section 3.5.4) is shown in Figure 3.10. The 5.08 mm (1/5") grid is the back side of a piece of engineering paper glued to a stiff backing. Care was taken not to disturb the camera after this grid photo was taken. The grid photo was scanned along with the ICV photographs. Two points on the grid were used as reference. We used points near the area of interest in order to minimize errors due to perspective and optical distortion. The number of pixels between those two points on the digital image was divided by the known physical distance between those two points to determine the conversion. This was done separately for the vertical and horizontal directions.

3.5 Validation

Here we will discuss the validation of the ICV. A number of tests were performed to determine the validity of the ICV. These tests included a digitally simulated velocity, a rotating disc, an ordinary jet of known velocity and turbulent pipe flow.

3.5.1 Digitally Simulated Velocity

The first test of the ICV was to simulate a pair of photos taken with some Δt between them. A black and white image of the synthetic fence jet was scanned into the computer. This image was then cropped twice with an offset

Figure 3.9: Grid photograph for SFJ experiments. Engineering paper provides the 5.08 mm (1/5") grid.

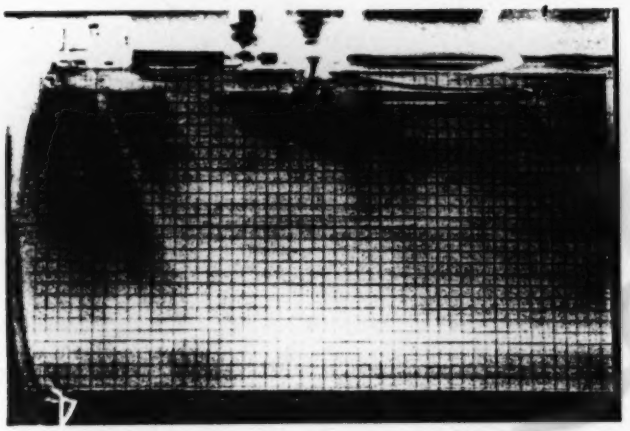

Figure 3.10: Grid photograph for turbulent pipe flow experiments discussed in Section 3.5.4. Engineering paper provides the 5.08 mm (1/5") grid.

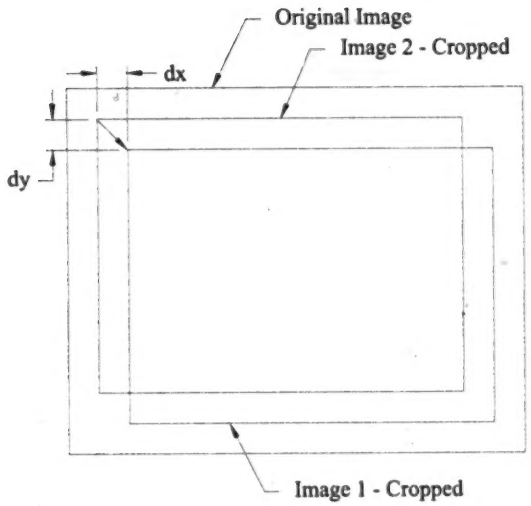

Figure 3.11: Digitally Simulated Velocity: Cropping for Translation. In order to simulate a velocity, the original image was cropped twice. The second image was cropped dx pixels to the right and dy pixels below the first image.

of 10 pixels both horizontally and vertically on the second crop as seen in Figure 3.11. This produced two images that were identical except that one was translated by 10 pixels horizontally and 10 pixels vertically. The was then performed on these images and the velocity field was found to be completely uniform and had the correct displacement of 10 pixels in each direction as seen in Figure 3.12. This test shows that the ICV will work perfectly if the images are completely identical with pure translation of an integer number of pixels. It is important to note that the translation of an integer number of pixels means that the two images were completely identical allowing the correlation to be perfect for the correct displacement. Also, because this was a pure translation case it is limited in its scope. The flows that are of interest always have some rotational component.

The second test involved the rotation of an image. As with the translation test described above, a black and white image was used. Using Microsoft Photo Editor, the image was rotated at an angle of 3.25°. The original image and the rotated image were then cropped to the same size maintaining the center of rotation in the image. ICV was then applied to these images as the red and blue components. The resulting velocity field is shown in Figure 3.14. The lengths of the vectors were correct to within 1 pixel for almost the entire field. There were however a few erroneous vectors. These erroneous vectors may be due to the fact that, unlike the translation test, the pixel values were not identical in the two images. This is because creation of the rotated image (unlike the translated image) requires the computer to interpolate. Also, the

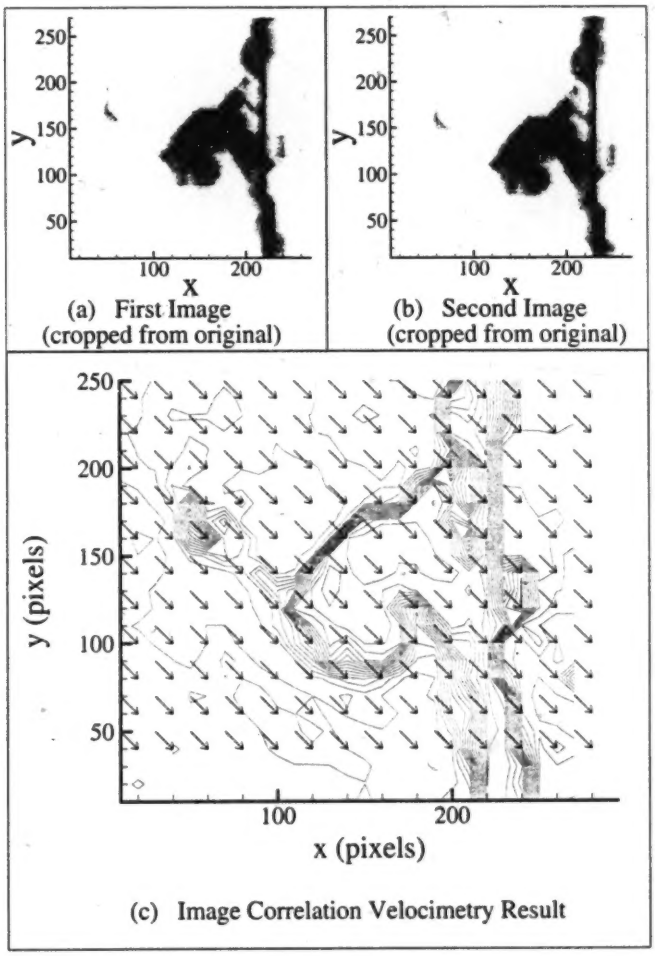

Figure 3.12: Digitally simulated velocity: translation ICV result. (a) Shows the first image. (b) Shows the second image. Both images were cropped from the same original image with an offset of 10 pixels in each direction. (c) Shows the image correlation velocimetry result from these two images overlaid on top of the contours of both images. The vectors are all exactly 10 in each direction.

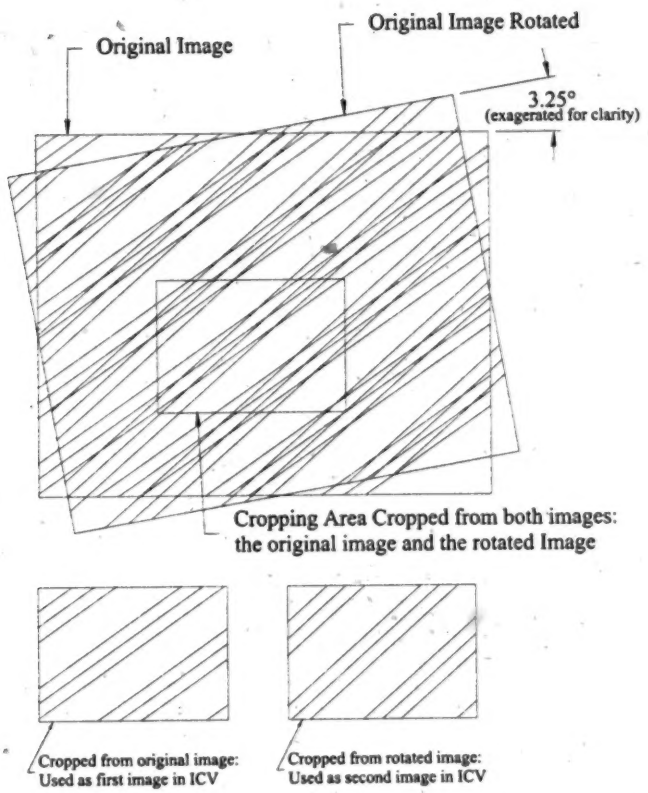
Original Image
Original Image Rotated
3.25°
(exagerated for clarity)
Cropping Area Cropped from both images:
the original image and the rotated Image
Cropped from original image:
Used as first image in ICV
Cropped from rotated image:
Used as second image in ICV

Figure 3.13: Digitally simulated velocity: cropping for rotation. In order to simulate a rotational flow, the original image was rotated 3.25°. Both images were then cropped to the same size.

pixel error becomes very large near the center of rotation since the pixel displacement goes to zero at the center of rotation.

3.5.2 Rotating Disc

In order to test the performance of the ICV in the environment in which it was intended to be used, a spinning disc was set up in the test section. This would account for errors due to the camera imaging, illumination, and timing of the strobes. A black and white matte printout of a scanned photograph[4] was pasted to the spinning disc to provide a similar image to the experiment. A set of photographs were taken using the entire ICV system including the two stroboscopes, timing box and colour filters. The angular velocity of the spinning disc was recorded and the photos were analyzed using the ICV program. The angular velocity of the disc was 5 radians per second. The results were quite good where there was sufficient image data to allow the ICV to work. Figure 3.15 shows a photograph. The resulting ICV result is shown in Figure 3.16. The ICV velocity was extracted along a line where the ICV appeared to work well and plotted against the true velocity calculated from the angular velocity. This is shown in Figure 3.17. Unfortunately there were reflections from the disc resulting in a poor image. At a typical velocity of 35 cm/s the error was found to be as low as 0% up to approximately 10% in the area of the photograph that appeared to work reasonably well. The percent error due to the resolution, or the pixel error (± 1 pixel), was

[4] A printout was used instead of the original photograph in an attempt to avoid the reflections that would certainly occur from a glossy photograph

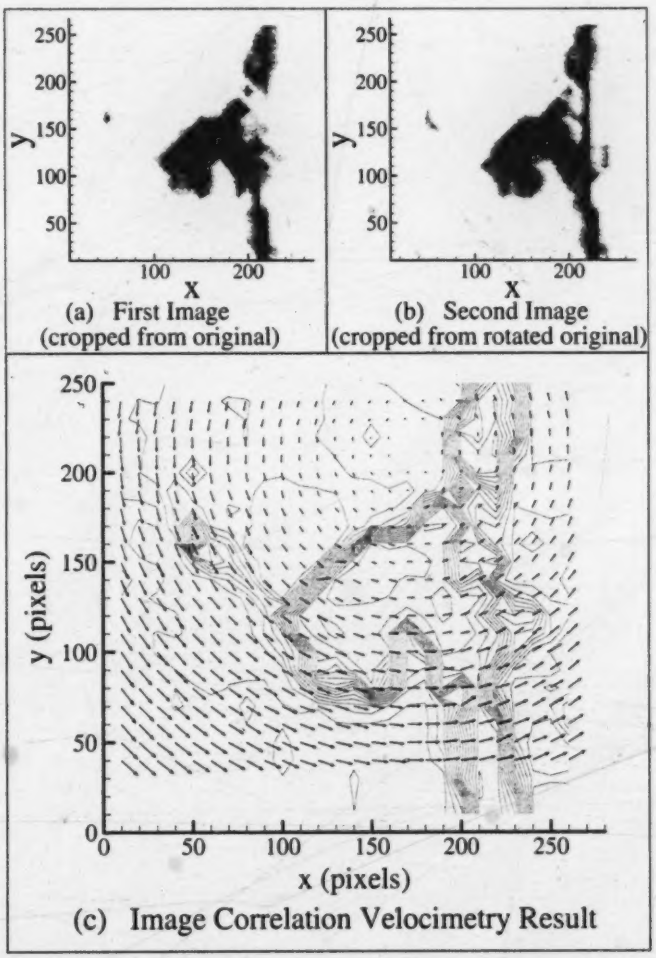

Figure 3.14: Digitally simulated velocity: rotation ICV result. (a) Shows the first image. (b) Shows the second image. The second image is the same as the first image except that it has been rotated 3.25° in the counter-clockwise direction. (c) Shows the image correlation velocimetry result from these two images overlaid on top of the image intensity intensity contours of both images.

approximately 8%. At a slightly lower velocity of approximately 25 cm/s, where the pixel error was approximately 11 %, the error was as high as 25 %. The errors are not entirely due to pixel error since the errors are higher than the pixel error.

3.5.3 Normal Jet Image Correlation Velocimetry Validation

In order to test the ICV on smoke-wire flow visualization photographs and in the experimental setting that it was intended to be used an ordinary jet was placed in the pipe rig.

The jet was produced using small diameter tubing hooked up to the building air supply. This pipe was positioned in the side of the pipe in the slot of the fence ring directed radially inwards in the pipe. With the pipe closed, creating a turbulent jet proved difficult. A recirculation of the flow is presumably responsible for causing the jet to remain laminar. The pipe was left open and the diameter of the jet nozzle was reduced to achieve a turbulent jet.

The velocity at the centerline of the jet was measured using a hot-wire anemometer. The complete ICV system was then used on this jet. Because the hot-wire would interfere with the ICV results, the hot-wire reading and the ICV could not be performed simultaneously. A ten second average was used for the hot-wire readings and a number of readings were taken. These values fluctuated by approximately ± 0.1 m/s. The results were compared to the hot-wire readings taken. Figure 3.18 shows one of the resulting images.

Figure 3.15: Photograph from spinning disc experiment. Printout of smoke-wire photograph was pasted onto spinning disc. The disc was placed in the pipe and rotated at an angular velocity of $5\frac{1}{4}$ radians per second. The blue stroboscope was fired 5 ms after the red stroboscope.

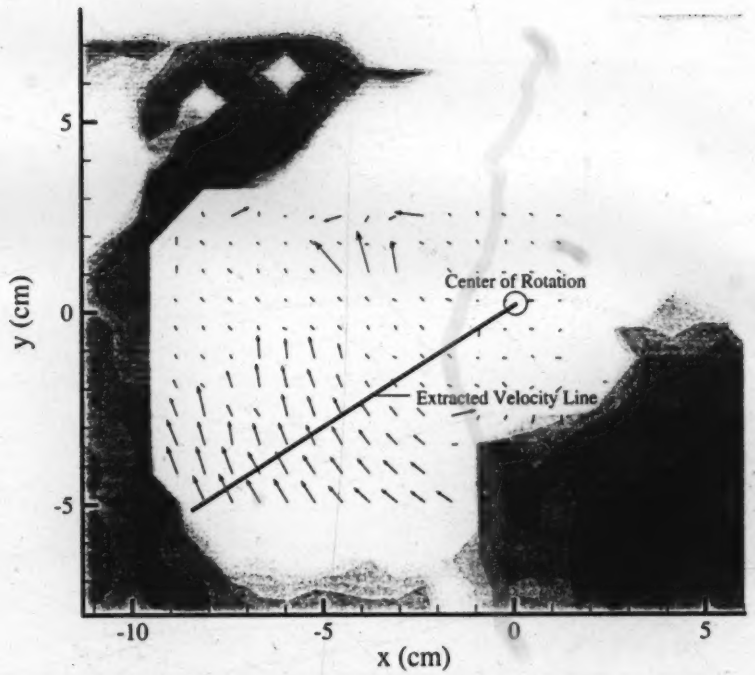

Figure 3.16: ICV result from spinning disc experiment. The disc was spinning at 5 radians per second. Reflections from the disc reduced the working area of the ICV result. The ICV velocity extracted along the line is compared with the actual velocity of the disc in Figure 3.17.

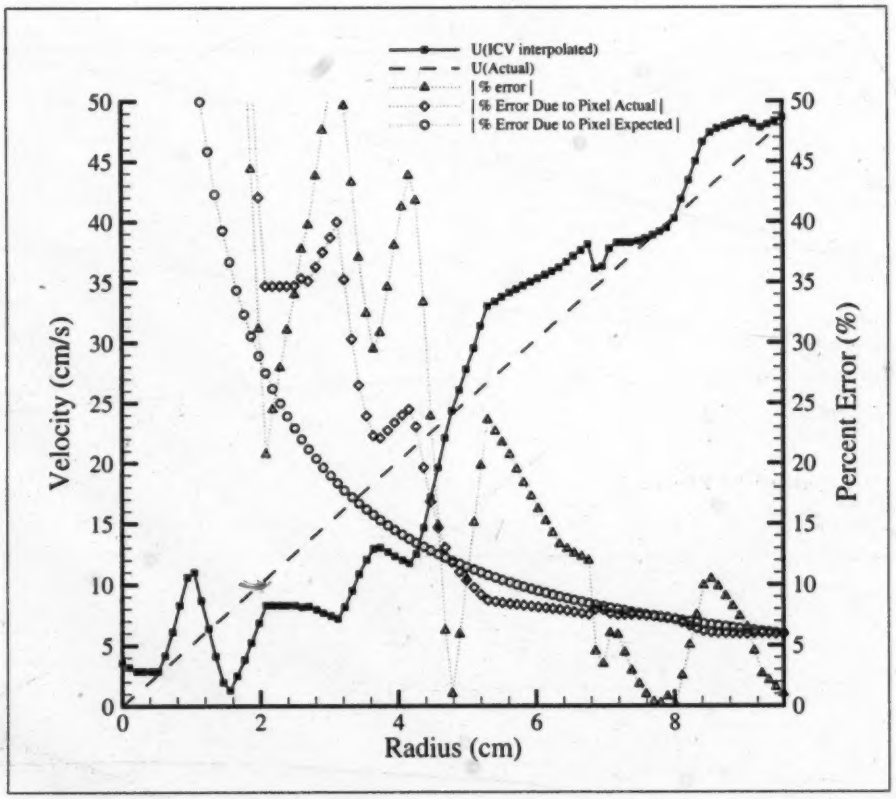

Figure 3.17: Velocity extracted along a line from spinning disc experiment. The ICV velocity shown here is extracted from the ICV result along the line shown in Figure 3.16. The disc was spinning at an angular velocity of 5 radians per second.

Figure 3.18: Photograph from normal jet image correlation velocimetry validation experiment. The blue stroboscope was fired 1 ms after the red stroboscope. The average velocity of the jet at the center of the pipe as measured using the hot-wire was 0.9 m/s.

The photographs were scanned using the two different scanners described in Section 3.3.3.4. As well, the Dust & Scratches filter also discussed in Section 3.3.3.4 was applied to the image digitized using the Minolta® Scanner. Therefore, there were three different sets of ICV results. One for the 1200 dpi HP® scanner and two for the 2820 dpi Minolta® scanner: one with the D&S filter applied and one without. The ICV result from the 2820 dpi scanned image with the filter applied is shown in Figure 3.19.

A set of three photographs with identical timing were taken and the ICV results for these images were averaged. When averaging the ICV results the average for each point does not include the point in the average if the velocity is zero. This is because points where the velocity is not calculated are assigned a velocity of zero. The averaged ICV result is shown in Figure 3.20.

The velocities extracted along the middle of the jet from the averaged ICV results for each of the three scanning techniques along with the hot-wire readings are shown in Figure 3.21. At the center of the pipe the results vary by approximately 15% between the different scanning techniques. The results with the 2820 dpi scanner are within the measurement error of the hot-wire.

3.5.4 Turbulent Pipe Flow

We investigated how well the ICV system would work on smoke-wire discrete streakline flows. To this point the ICV had been used only on very turbulent flows in which the smoke has become a cloud of smoke rather than the distinct

Figure 3.19: Image correlation velocimetry result from normal jet image correlation velocimetry validation experiment. Image scanned using 2820 dpi scanner and filtered with Adobe Dust & Scratches Filter. The average velocity of the jet at the center of the pipe as measured using the hot-wire was 0.9 m/s.

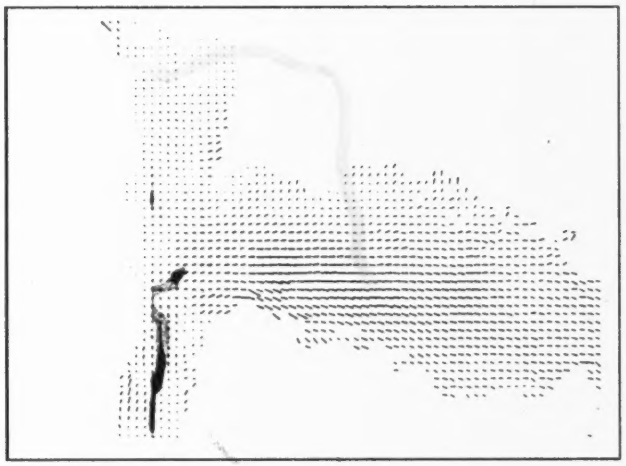

Figure 3.20: Averaged image correlation velocimetry result from normal jet image correlation velocimetry validation experiment. Images scanned using 2820 dpi scanner and filtered with Adobe Dust & Scratches Filter. Result averaged over three images. The average velocity of the jet at the center of the pipe as measured using the hot-wire was 0.9 m/s.

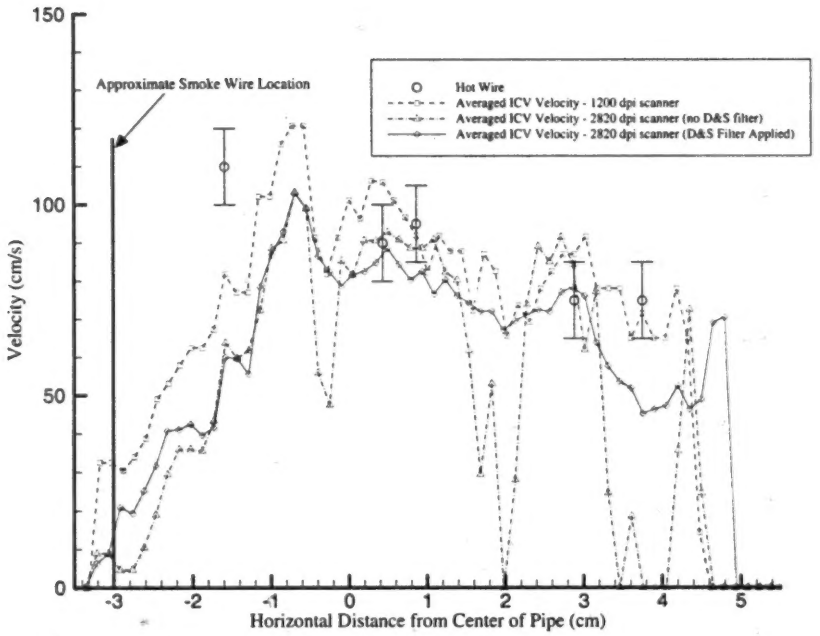

Figure 3.21: Averaged ICV velocity along centerline from normal jet ICV validation experiment. Hot-wire error bars are due to fluctuations in the hot-wire reading. ICV velocities are averaged over three photographs.

Figure 3.22: Photograph from turbulent pipe flow experiment. The blue stroboscope was fired 2 ms after the red strobe. The average velocity along the centerline of the pipe as measured using the hot-wire was 1.3 m/s.

streaklines that are normally associated with smoke-wire flow visualization.

The pipé centerline velocity was measured using a hot-wire anemometer and a set of 8 photographs were taken for 3 different Δt's: 1 ms, 2 ms, and 5 ms. The centerline velocity in the pipe was 1.3 meters per second. Figure 3.22 shows one of the photographs with a Δt of 2 ms. The ICV results from the 8 photographs were averaged and compared to the hot-wire velocity. Figure 3.23 shows the ICV results for the case where the Δt was 2 ms. The pixel displacement was approximately 36 pixels in the centerline for the photographs where Δt was 2 ms. Figure 3.24 shows a comparison

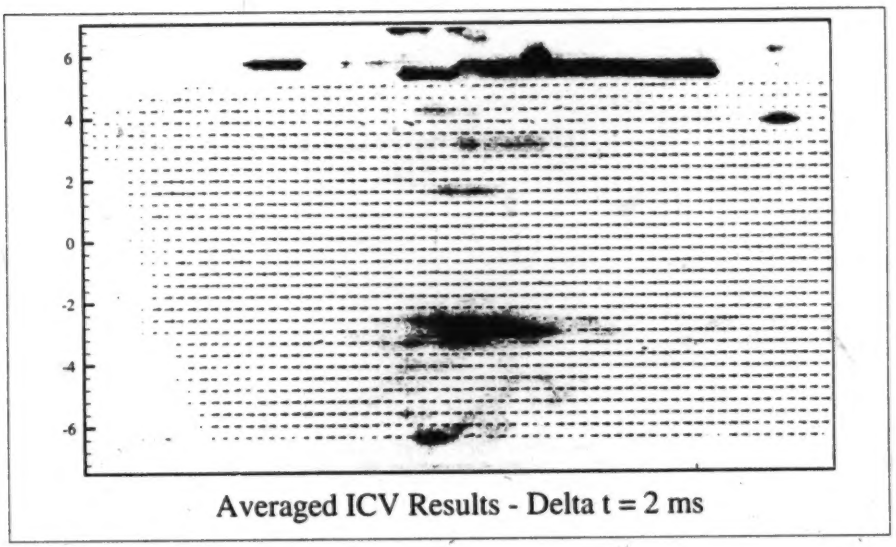

Figure 3.23: Image Correlation Velocimetry results from turbulent pipe flow experiment. Average ICV from 8 photographs with a Δt of 2 ms. The average velocity along the centerline of the pipe as measured using the hot-wire was 1.3 m/s.

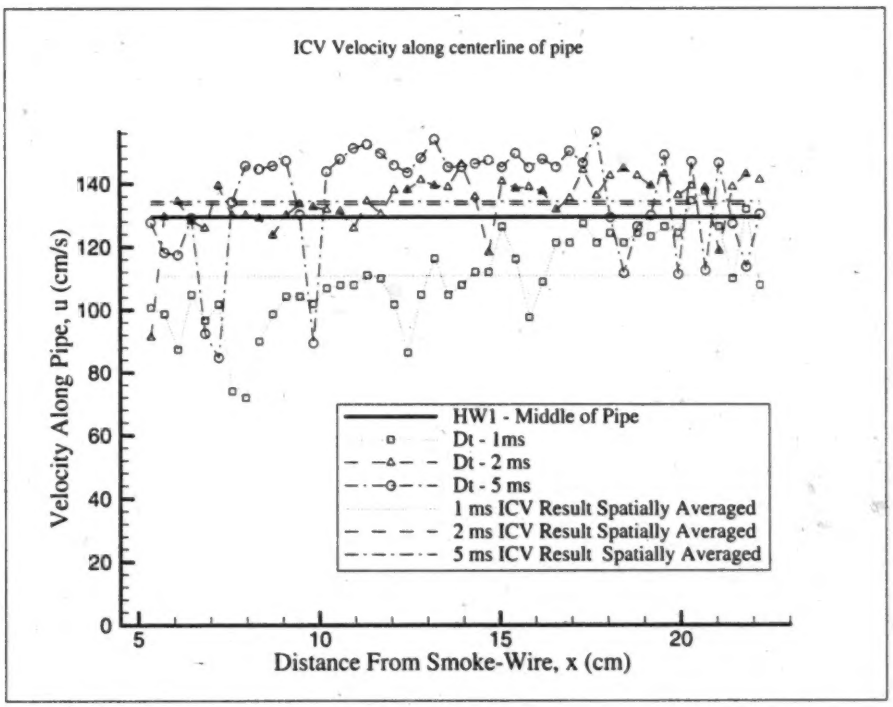

Figure 3.24: Image correlation velocimetry and hot-wire centerline velocity from turbulent pipe flow experiment. ICV velocity spatially averaged to increase the number of realizations used in averaging

between the measured hot-wire velocity and the velocity calculated using ICV. The ICV result was averaged spatially along the pipe centerline. This resulted in an effective number of approximately 400 averaged realizations. The errors for these averaged results are given in Table 3.1. For the 2 ms

Table 3.1: Turbulent pipe flow: Comparison of percent error and pixel error

Δt	Δx (pixels)	% error	pixel error
1 ms	18	−14%	±5.5%
2 ms	36	3%	±2.8%
5 ms	90	4%	±1.1%

Δt case the error is approximately the same as the pixel error of 2.8%. The larger error found with the 1 ms Δt case cannot be explained solely with its increased pixel error. From this data it appears that the optimum pixel displacement to minimize the ICV errors is around 36 pixels for this type of flow. The ICV velocity along the pipe shows significant fluctuations, even when averaged over 8 pictures. To obtain good accuracy with this technique, a very large number of realizations is required. The errors listed in Table 3.1 effectively had approximately 400 realizations.

3.5.5 Validation Summary

A series of experiments were performed to validate the performance of the ICV technique developed. These experiments were designed to test the functioning of the code to the performance of the complete system. The tests were as follows:

Digitally Simulated Translation - Two images were created by cropping the same original image with a slight displacement. ICV was then applied to these images. This tested the operation of the code under ideal conditions.(see Section 3.5.1)

Digitally Simulated Rotation - Similar to Digitally Simulated Translation except that there was a rotational component.(see Section 3.5.1)

Rotating Disc - An image was pasted to a rotating disc of known angular velocity and this disc was placed in the test section. The complete ICV system including the photography system was then applied to this known velocity. This tested the complete system.(see Section 3.5.2)

Normal Jet - A normal fluid jet was positioned in the test section and the complete ICV system was applied to it. The results were compared to hot-wire measurements along the centerline of the jet. This tested the performance of the complete ICV system when applied to smoke with a similar appearance to the SFJ.(see Section 3.5.3)

Turbulent Pipe Flow - The complete ICV system was applied to turbulent pipe flow. A hot-wire was used to measure the centerline velocity in the pipe. This tested the ICV system on smoke-wire streaklines.(see Section 3.5.4)

3.6 Conclusions

An image correlation velocimetry (ICV) technique was developed to study the jet that is created when a fence is placed in an oscillating flow in a pipe. This ICV method involves the use of stroboscopes of different colours to allow separation of the images on one film slide that were taken at different times.

The filters used to produce the coloured lighting were very important to allowing the images to be extracted. High quality light filters that are designed for colour separation work were required to ensure that each component of the image was separate. Light filters that are not designed for colour separation work allow some of one component of the image to be visible in the other component.

The positioning of the light sources was very important to ensuring that the images were identical for simultaneous stroboscope photographs. The ideal case is for the stroboscopes to be in the same physical location so that precisely the same area is illuminated. While it is impossible for the stroboscopes to occupy the same space simultaneously, through the use of a beam-splitter the stroboscopes appear to be in the same place at the same time. An innovative apparatus was constructed to ensure that the beam splitter and the stroboscopes are positioned to allow the stroboscopes to appear to occupy the same space simultaneously.

The method of digitizing the photographs is a very important part of the process. With a higher resolution scanner the grain of the photograph

would interfere with the performance of the ICV. The ICV would 'lock' on to the grain of the film which has approximately the same length scale in all components of the image and report a velocity of zero. If the resolution of the scanning is too low then the pixel error is increased. The effects of the grain on the ICV performance can be reduced through the use of image processing. With the use of a computational filter, the grain of the image was reduced.

The code could be accelerated significantly through the use of a multi-grid scheme. By reducing the image resolution numerically and performing ICV on the reduced resolution image we obtain a better initial guess for the higher resolution thereby reducing the required search area. Two levels of resolution reduction were implemented and the solution remained unchanged. For some test cases the running time of the code was reduced from over 24 hours to approximately 10 minutes.

The correlation-based correction used by Hart (2000) for PIV error correction was used with the ICV algorithm. This method can be used to improve the ICV result by eliminating some of the errors.

By digitally translating and rotating images, we have shown that the ICV code produced perfect results for translation if the images that are input are identical with translation of an integer number of pixels. For rotation, the result is still very good but some errors started to appear. Also, near the center of rotation, the pixel error became very large.

Through the use of a spinning disc, we tested the entire ICV system

including the photographic system, the beam splitter apparatus, the coloured lighting, and even the transparent pipe optics. Where the ICV worked it worked quite well. The error was found to be less than 10% for a velocity of around 0.35 m/s. At lower velocities the error was higher but at higher velocities the error was reduced. The errors at lower velocities were higher than the pixel error indicating that they were not caused by pixel error. At higher velocities, the errors appeared to be close to pixel error.

For flows that are similar to the SFJ where the smoke is mixed rapidly and becomes a cloud of smoke rather than distinct streaklines, the ICV worked reasonably well near the center of the pipe where the error was found to be approximately 15%.

The ICV worked very well when applied to smoke-wire streakline photographs of a turbulent pipe flow that had well defined streaklines. The error was as low as 4% when the data is averaged over a sufficient number of realizations.

Acknowledgements for Chapter 3

Dr. Tony Chen is thanked for writing the ICV code. We thank Michelle Vigeant who, as a summer student, began researching the ICV technique. Thanks also to Professor Dimotakis for help at the beginning of this endeavor. Finally, thanks to the VFD Group for all of the support throughout this project: Andrew Coward, Dave deJong, and John Diep.

BIBLIOGRAPHY

Adrian, R. (1991). Particle-imaging techniques for experimental fluid mechanics. *Annual Review of Fluid Mechanics*, 23:261–304.

Hart, D. (2000). Piv error correction. *Experiments in Fluids*, 29:13–22.

Murakami, E. and Papamoschou, D. (2000). Eddy convection in coaxial supersonic jets. *AIAA*, 38:628–635.

Papamoschou, D. and Bunyajitradulya, A. (1997). Evolution of large eddies in compressible shear layers. *Physics of Fluids*, 9:756–765.

Reza, M., Kim, J., Satoru, S., Okazaki, K., and Tamura, S. (1999). A scaled multigrid optical flow algorithm based on the least rms error between real and estimated second images. *Pattern Recognition*, 32:657–670.

Tokumaru, P. and Dimotakis, P. (1995). Image correlation velocimetry. *Experiments in Fluids*, 19:1–15.

CHAPTER 4

CONCLUSIONS AND FURTHER RESEARCH

4.1 Conclusions

A type of jet that we have chosen to call a synthetic fence jet (SFJ) has been confirmed and explored. This jet is created when a fence is introduced into an oscillating flow. The vortices that are shed from the fence interact with each other and create a jet of fluid that is directed away from the fence.

An image correlation velocimetry (ICV) technique was developed to study this jet. The computational method used was adapted from Papamoschou and Bunyajitradulya (1997). This ICV technique involves the use of two different coloured stroboscopes exposing a single colour slide rather than two separate slides or negatives . After digitizing the slide, the colour components can be digitally extracted to obtain the two images required. This method was validated through a number of experiments. It was found to work very well on smoke-wire streaklines in turbulent pipe flow.

ICV results for the SFJ indicate that the velocity ratio (jet velocity di-

vided by the velocity amplitude of the forcing) ranges from approximately 0.14 to approximately 0.94 for a Reynolds number of 620. The Strouhal number at which the maximum velocity ratio was obtained was 1.68. The maximum average velocity ratio for a Reynolds number of 620 was found to be 0.55 at a Strouhal number of 1.8.

The frequency of the large scale structures in the jet was estimated to be approximately $1/20^{th}$ of the forcing frequency. This may be explained by approximately 4 pairings of the created vortices. Alternatively, the jet could be laminar initially and then develop a lower frequency instability as it moves away from the fence.

For the circular pipe and fence used in the experiments, the jetting occurred only near the middle of the fence and not along its entire length. This is due to the recirculating nature of the flow due to the pipe boundary.

We also found that the SFJ could be vectored along the pipe axis by altering the forcing waveform. A theory that is based on the Biot-Savart law of vortex dynamics has been developed to explain this vectoring phenomenon.

4.2 Further Research

There are many additional experiments that could be performed to learn more about the SFJ and the ICV technique.

There is still much to be learned about the SFJ. We used a fence in a circular pipe with air as the fluid. Following are a number of possible suggestions for future experiments:

- Further testing of the vectored SFJ using ICV to determine the jet velocities.
- Analyze jet velocity profiles from the existing ICV data.
- Increase the number of data points available by adding extensions to the Pulsating Pipe Facility. This would alter the resonant frequency of the pipe and allow jets to be produced at more frequencies.
- Use a rectangular cross-section wind tunnel. This may reduce the three-dimensionality of the flow structure. Of interest would be whether the jetting occurs along the entire length of the fence or just in the middle as in the case of the circular fence.
- Use different geometries of 'fences' such as triangular wedges (in sectional view along pipe axis), curved wedges[1], and half cylinders.
- Use a flexible material for the fence. This might allow it to behave more like a fish's tail and rotate.
- Place a flat plate in the middle of an oscillating flow so that there would be two edges where jets could be produced on either side of the flat plate.
- Use a U-tube apparatus to allow testing to be done in water.

[1] Wedges have been constructed in the VFD Lab and there have been some experiments performed with them already.

There is also a significant amount of work that can be done to improve the ICV technique as well as a number of experiments that can be done using the ICV technique.

The most significant improvement to the ICV method used would be to use a digital camera to obtain the images. There would be a dramatic reduction in the amount of time lag between performing an experiment and seeing the results. When using film, the film had to be developed which takes about one work day. The film had to be digitized which took a couple of hours per roll to do. Using a digital camera, an image could be processed and an ICV result found within minutes rather than days.

The ICV method can be tried on a variety of flow visualization techniques and on a variety of flows. A current graduate student will be performing an experiment using the ICV on hydrogen bubble flow visualization in turbulent pipe flow. It would be interesting to try the ICV code on existing photographs from PIV experiments and other consecutive image photographs.

There are some parts of the code that use significantly more memory than they need to and that could be optimized to improve the speed of the code. The user interface could be improved by adding a graphical user interface to make it more user friendly.

BIBLIOGRAPHY

Papamoschou, D. and Bunyajitradulya, A. (1997). Evolution of large eddies in compressible shear layers. *Physics of Fluids*, 9:756–765.

Appendix A

ICV Initialization File

There are a number of parameters that can be changed to suit the data being analyzed and the output desired. These parameters are placed in an initialization file to allow them to be easily modified. In this section we will describe the initialization file that is used with the code and explain what the parameters are and how they affect the code. A sample initialization file is shown in Table A.1.

Velocity Output Skip

These are parameters which determine the distance between calculated velocity vectors. It also determines the distance between the extracted pixel brightness values for the output file. For the image correlation velocimetry calculations, all of the pixels are used in the calculations but in order to reduce file size, not all of the pixel values are output.

Maximum Velocity (High Res)

Table A.1: Sample Initialization File

12	//	velocity output skip (i, in pixels)
12	//	velocity output skip (j, in pixels)
5	//	max velocity (high res)(in pixels)
36	//	correlation window half size (i)
36	//	correlation window half size (j)
6	//	deviation of correlation tables
1	//	calibration parameter (alfa)
0	//	calibration parameter (beta)
35	//	calibration parameter (threshold)
0.0	//	calibration parameter (corrthreshold)
100	//	istart - pseudo cropping
500	//	iend
100	//	jstart
500	//	jend
1	//	number of tables (1,2, or 4)
5	//	max velocity (half res)(in high res pixels)
20	//	max velocity (quarter res)(in high res pixels)

This parameter determines how far the program searches for a solution. This is the distance from the initial guess which is passed from the half resolution solution.

Correlation Window Half-Size

These parameters determine the size of the correlation window. The correlation window defined by the correlation window half size (i) pixels in each direction horizontally from the center and the correlation window half size (j) in each direction vertically from the center.

Deviation of the Correlation Tables

This parameter determines the deviation of the correlation tables for

the correlation based correction method discussed in Section 3.4.2. If this value is set to 0 then the correlation based correction method is not used.

Calibration Parameters Alpha and Beta

These parameters are not used any more as they were determined to make no difference. They were used to balance the differences between the intensity of the Red and Blue light in the images. A reference photo was taken with the red and blue stroboscopes fired simultaneously and a calibration code was run that performed a linear fit between the red and blue pixel values. The blue pixel values were adjusted to obtain the minimum difference between the red and blue images. These parameters have no effect on the code because the code uses the deviation of the intensity from the spatial average.

Calibration Parameters Threshold

This parameter gives the pixel value below which the image correlation velocimetry will not be performed for a particular point in the image. If the pixel value is too low then there is insufficient data to correlate. Some images have more background noise than others so this parameter can be adjusted to prevent image correlation velocimetry from being performed on this background noise.

Calibration Parameters Corrthreshold

This parameter is used to discard image correlation velocimetry solutions where the correlation is too low for the solution to be trusted. A perfect correlation is 1.

Pseudo Cropping Parameters

These parameters are used to limit the portion of the image that image correlation velocimetry is performed on without actually cropping the image. The images contain more information than just the smoke. These parameters allow the image correlation velocimetry to be performed on only the area of interest and not on any extraneous information in the image. This reduces the running time of the code.

Number of Tables

This parameter determines the number of correlation tables used when using the correlation based correction method. If this parameter is set to 2 then 2 correlation tables offset horizontally are used. The amount they are offset is determined by the deviation of the correlation tables parameter described above. If the number of tables parameter is set to 4 then 4 tables are used. In this case 2 tables are offset in the horizontal direction and 2 tables are offset in the vertical direction. If it is set to 1 then the correlation based correction method is not used.

Max Velocity (Half Resolution)

This parameter determines the distance from the initial guess passed

from the quarter resolution solution to be searched in the half resolution portion of the code. It is in half resolution pixels.

Max Velocity (Quarter Resolution)

This parameter determines the distance to search in quarter resolution pixels during the initial quarter resolution calculation.